ORIGINAL ARTICLE

gebiology   WILEY

Identifying microbial life in rocks: Insights from population morphometry

Joti Rouillard[1] [iD] | Juan Manuel García-Ruiz[2] [iD] | Linda Kah[3] | Emmanuelle Gérard[1] | Laurie Barrier[4] | Sami Nabhan[1] [iD] | Jian Gong[1] [iD] | Mark A. van Zuilen[1] [iD]

[1]Equipe Géomicrobiologie, Université de Paris, Institut de Physique du Globe de Paris, CNRS, Paris, France

[2]Laboratorio de Estudios Cristalográficos, Instituto Andaluz de Ciencias de la Tierra, Consejo Superior de Investígacıones Cientificas–Universidad de Granada, Granada, Spain

[3]Department of Earth and Planetary Sciences, University of Tennessee, Knoxville, TN, USA

[4]Equipe Tectonique et Mécanique de la Lithosphère, Université de Paris, Institut de Physique du Globe de Paris, CNRS, Paris, France

Correspondence
Joti Rouillard, Equipe Géomicrobiologie, Institut de Physique du Globe de Paris, 1 rue Jussieu, 75238 Paris cedex 5, France.
Email: joti.rouillard@gmail.com

Funding information
European Research Council (ERC) under the European Union's Horizon 2020 Research and Innovation Program, Grant/Award Number: 646894; ERC Seventh Framework Programme FP7/2007-2013, Grant/Award Number: 340863; Ministerio de Economía y Competitividad of Spain, Grant/Award Number: CGL2016-78971-P

Abstract

The identification of cellular life in the rock record is problematic, since microbial life forms, and particularly bacteria, lack sufficient morphologic complexity to be effectively distinguished from certain abiogenic features in rocks. Examples include organic pore-fillings, hydrocarbon-containing fluid inclusions, organic coatings on exfoliated crystals and biomimetic mineral aggregates (biomorphs). This has led to the interpretation and re-interpretation of individual microstructures in the rock record. The morphologic description of entire populations of microstructures, however, may provide support for distinguishing between preserved micro-organisms and abiogenic objects. Here, we present a statistical approach based on quantitative morphological description of populations of microstructures. Images of modern microbial populations were compared to images of two relevant types of abiogenic microstructures: interstitial spaces and silica–carbonate biomorphs. For the populations of these three systems, the size, circularity, and solidity of individual particles were calculated. Subsequently, the mean/*SD*, skewness, and kurtosis of the statistical distributions of these parameters were established. This allowed the qualitative and quantitative comparison of distributions in these three systems. In addition, the fractal dimension and lacunarity of the populations were determined. In total, 11 parameters, independent of absolute size or shape, were used to characterize each population of microstructures. Using discriminant analysis with parameter subsets, it was found that size and shape distributions are typically sufficient to discriminate populations of biologic and abiogenic microstructures. Analysis of ancient, yet unambiguously biologic, samples (1.0 Ga Angmaat Formation, Baffin Island, Canada) suggests that taphonomic effects can alter morphometric characteristics and complicate image analysis; therefore, a wider range of microfossil assemblages should be studied in the future before automated analyses can be developed. In general, however, it is clear from our results that there is great potential for morphometric descriptions of populations in the context of life recognition in rocks, either on Earth or on extraterrestrial bodies.

1 | INTRODUCTION

The use of morphology as a tool for identification of microfossils, especially in the most ancient records, has been fraught with difficulties. Early life forms lacked sufficient morphologic complexity to be easily distinguished from abiogenic structures, such as pore-fillings, interstitial spaces between crystals, air bubbles, and fluid inclusions. Furthermore, certain abiotic self-organized structures, including silica–carbonate biomorphs (Carnerup, 2007; García-Ruiz et al., 2003; Rouillard, García-Ruiz, Gong, & Zuilen, 2018), chemical gardens (McMahon, 1916), carbon–sulfur biomorphs (Cosmidis & Templeton, 2016), or manganese oxide biomorphs (Muscente, Czaja, Tuggle, Winkler, & Xiao, 2018) also have the potential to create a variety of shapes, including spheroids, framboids, helicoids, or filaments that resemble individual cells or clusters of cells. The shapes adopted by microbial cells and colonies are therefore not unique to living systems. Besides, the interpretation of ancient samples must consider that post-depositional geologic processes, that could have introduced secondary abiogenic structures, may affect the morphology of fossilized life. As a consequence, the identification of ancient microfossils oftentimes remains controversial. The most well-known controversy concerns the occurrence of filamentous microstructures in the 3.5 Ga Apex Chert. Interpreted initially as filamentous micro-organisms (Schopf, 1993; Schopf, Kitajima, Spicuzza, Kudryavtsev, & Valley, 2018; Schopf & Kudryavtsev, 2009, 2012; Schopf, Kudryavtsev, Agresti, Wdowiak, & Czaja, 2002; Schopf, Kudryavtsev, Sugitani, & Walter, 2010) preserved in sedimentary chert, these structures have been subsequently reinterpreted as infilling in the microporous structure of recrystallized silica (Brasier et al., 2002, 2005, 2011), as exfoliated mica crystals (Wacey, Saunders, Kong, Brasier, & Brasier, 2015) in a hydrothermal chert vein, and have been compared to silica–carbonate biomorphs known to precipitate within silica-rich, alkaline media (García-Ruiz et al., 2003).

In order to answer these difficulties, specific criteria have been proposed to assess the biologic origin of potential microfossils in rocks (Brasier & Wacey, 2012; Buick, 1990; Schopf, 1983; Vago et al., 2017). These biogenicity criteria require that (a) microstructures occur in a sedimentary rock of constrained age, (b) are hollow and contain a mineral filling, (c) include traces of altered organics, (d) display a biologic-like shape, and (e) occur spatially associated with similar specimens reflecting a biologic population. In recent years, the evaluation of biogenicity criteria has been greatly improved with the high-resolution, in situ chemical and structural characterization of potential microfossils and of their mineral matrix (Baghekema et al., 2017; Brasier, Antcliffe, Saunders, & Wacey, 2015; Delarue et al., 2016, 2018; Fadel, Lepot, Busigny, Addad, & Troadec, 2017; Guo, Peng, Czaja, Chen, & Ta, 2018; House, Oehler, Sugitani, & Mimura, 2013; Javaux, Knoll, & Walter, 2004; Kempe et al., 2005; Lepot et al., 2017; Pang et al., 2013; Schopf et al., 2018, 2002; Schopf & Kudryavtsev, 2009; Wacey, Kilburn, Saunders, Cliff, & Brasier, 2011; Wacey et al., 2012, 2015; Williford et al., 2013). This characterization also facilitated the determination of the indigenous character of a carbonaceous microfossil, enabling the exclusion of modern organic contaminants and modern endoliths.

We extend here the morphologic approach to entire populations of microstructures. This will specifically bring more light and precision to one of the aforementioned criteria of biogenicity: the association of individual structures representing a biologic population. A critical question to address is whether populations of abiogenic structures such as interstitial spaces and biomorphic mineral aggregates can be quantitatively distinguished from populations of micro-organisms. If it can be shown that this is possible, preliminary tests of biogenicity can be made without the use of complex and expensive in situ analytical techniques.

One possible approach to discriminate between different types of populations of microstructures is by using artificial intelligence. Automated classification has been made possible with the use of multivariate analyses and has improved with the development of machine learning (Bishop, 2006; Domingos, 2012; McLachlan, 2004; Pedregosa et al., 2011; Robert, 2014; Snoek, Larochelle, & Adams, 2012). This technique has been applied in a variety of fields, including igneous petrology (facies recognition; Młynarczuk, Górszczyk, & Ślipek, 2013), entomology (taxon recognition; MacLeod, Benfield, & Culverhouse, 2010), palynology (taxon recognition; Holt, Allen, Hodgson, Marsland, & Flenley, 2011), and forensic science (face and fingerprint recognition; Etemad & Chellappa, 1997; Farina, Kovacs-Vajna, & Leone, 1999). In theory, using an assemblage of example images for biogenic and biomimicking populations, machine learning could be used to empirically distinguish populations of micro-organisms from abiogenic populations. However, machine learning approaches usually necessitate a large number of images, which may be difficult to obtain for the populations of relevance here. Additionally, many machine learning algorithms make it difficult to discretely identify the decisive criteria that distinguish the systems.

Another approach constitutes the quantitative description of the morphology (or morphometry) of entire populations of microstructures. The shapes and sizes of individual biological structures may be mimicked by abiogenic processes, but the controls exerted by biology on the morphology, and therefore the variation of, and correlation between, morphology-describing parameters could constitute more robust criteria for biogenicity. Morphometry has evolved considerably over the last decades, in large part because of the rapid increase in computing power. Softwares for image analysis are now used routinely to extract size or shape-describing features of objects (Adams & Otárola-Castillo, 2013; Adams, Rohlf, & Slice, 2004; Doube et al., 2010; Ferreira et al., 2014; Papadopulos et al., 2007; Rappaz et al., 2005), and such measurements have been applied to different fields: neurosciences (Bora, Fornito, Pantelis, & Yücel, 2012; Ferreira et al., 2014; Rajkowska et al., 1999), phanerozoic micropaleontology, food microstructure (Aguilera, 2005), medicine (Karakas & Kavaklı, 2005), and basin topography (Srinivasa Vittala, Govindaiah, & Honne Gowda, 2004), among others. Parameters such as size distributions have been examined for decades in the context of Precambrian life (Barghoorn & Tyler, 1965; Butterfield & Chandler, 1992; Knoll &

Barghoorn, 1977; Köhler & Heubeck, 2019; Schopf & Barghoorn, 1967; Schopf et al., 2010; Sugitani et al., 2007, 2010; Sugitani, Mimura, Nagaoka, Lepot, & Takeuchi, 2013; Wacey et al., 2011). Very recently, a study of the morphologic variation in two specific populations of organic microstructures from the 3.4 Ga Strelley Pool formation was conducted, indicating significant differences between populations and the existence of distinct sub-populations, with potential important paleoecological implications (Sugitani et al., 2018).

To the best of our knowledge, there is no general survey of the potential of statistical morphometrics for life recognition. One of the most important outcomes of morphometric studies is the construction of morphospaces–theoretical spaces in which axes represent continuous morphology-describing parameters. As far as we know, morphospaces haves been used in paleontology for individuals of a specific biologic group. For instance, in the seminal work conducted on ammonoid shells by Raup, 1967, an individual is represented by a point. It has been found that, in any morphospace, the regions occupied by individuals from a specific biologic group are restricted by developmental and adaptive constraints. In this study, we extend the concept of morphospace to the population level; that is, populations are represented by a single point in these "population" morphospaces. We make the hypothesis that the occupancy of population morphospaces by microbial communities depends on individual-scale processes (development, adaptation) but also on population-scale processes (ecologic relationships, environmental forcings). In this study, we critically test whether populations of specific abiogenic objects show fundamentally different morphometric characteristics in comparison with populations of modern micro-organisms (single-strain and multiple-strain communities). Two different types of abiogenic objects were chosen: interstitial spaces between clasts in sedimentary rocks and silica–carbonate biomorphs. The importance of silica–carbonate biomorphs for micropaleontology has been put forward in previous studies (García-Ruiz, Carnerup, Christy, Welham, & Hyde, 2002; García-Ruiz et al., 2003; Rouillard et al., 2018). They display a wide range of life-like morphologies; during the Archean, they may have been formed—and preserved—in the same hydrothermal environments where life emerged and first evolved. As a consequence, they represent a material of choice for the current study. Interstitial spaces, especially those in spherulitic or botryoidal chert fabrics, display a continuum of shapes that may also be mistaken for degraded microfossils (Brasier et al., 2002, 2005). In this proof of concept study, and for practical reasons, the system of clastic interstitial spaces was chosen. They are genetically different from interstitial spaces in spherulitic or botryoidal chert fabrics, but they have important morphologic similarities. These three systems—interstitial spaces, biomorphic mineral aggregates, and microbial cells–are compared using the statistical distributions of size and shape-describing parameters (circularity, solidity), and pattern-describing parameters (fractal dimension and lacunarity). In addition, correlation studies and multivariate analyses are conducted in order to maximize discrimination between the three systems. The method devised is then tested on well-preserved, silicified microfossil assemblages from the 1.0 Ga old Angmaat Formation (Bylot group, Baffin Island, Canada).

Based on this test, the limits and potential applications of statistical morphometry are discussed.

2 | MATERIALS AND METHODS

2.1 | Description of the images used

Three populations of microstructure are compared in the context of this study: (a) interstitial spaces, (b) silica–carbonate biomorphs, and (c) microbial populations. This study was performed using representative images for each system (presented in full in Figures S1–S6). Examples of images from the different systems are shown in Figures 1–3.

2.1.1 | System 1: Interstitial spaces in clastic sedimentary fabrics

This system is represented by eight images taken on five different samples of sandstone and one sample of limestone (Figures S1 and S2).

The first three sandstones contain ferruginous cement within interstitial pore space, the opacity of which allows ready identification of pore space under plane-polarized light. The first sandstone (Figure 1a; Figure S1A) consists of a fine- to medium-grained detrital sediment composed of angular quartz, together with mica. Micaceous grains are commonly deformed by compaction of quartz. The second sandstone (Figure 1b, Figures S1C and S2C,D) consists of a medium-grained detrital sediment composed of subangular quartz and feldspar. The third sandstone (Figure S2E) corresponds to a medium- to coarse-grained detrital sediment composed of angular to subangular quartz, feldspar, and mica mineral grains, as well as lithic fragments composed of volcanic rock and glass.

The next two sandstone samples add additional complexity. The fourth sandstone (Figure S2A) consists of a medium- to coarse-grained detrital sediment composed of angular to subangular quartz and feldspar mineral grains, detrital calcite, with macrocrystalline calcite cement filling most of the interstitial spaces between the grains. In plane-polarized light, the presence of calcite as both detrital grains and as interstitial cement complicates the distinction between the grains and the initial porosity. Similarly, the last sandstone (Figure S1B) consists of a medium-grained clastic sediment mainly composed of subangular quartz, feldspar, and mica mineral grains, a variety of lithic fragments, and (rare) bioclasts consisting of echinoderm and bryozoan skeletal fragments. Bioclasts are broken and abraded and do not retain their primary biologic shape. A macrocrystalline calcite cement fills most of the interstitial spaces between the grains. Here again, in plane-polarized light, a number of clasts appear very similar to the cemented pores, which complicates the distinction between the grains and the initial porosity. These two samples were also used to investigate the robustness of the method regarding segmentation quality (see Sections 2.2 and 4.2.2).

Finally, a single limestone sample (Figure S2B) was analyzed. This sample consists of an oolitic and pelletal grainstone, associated with
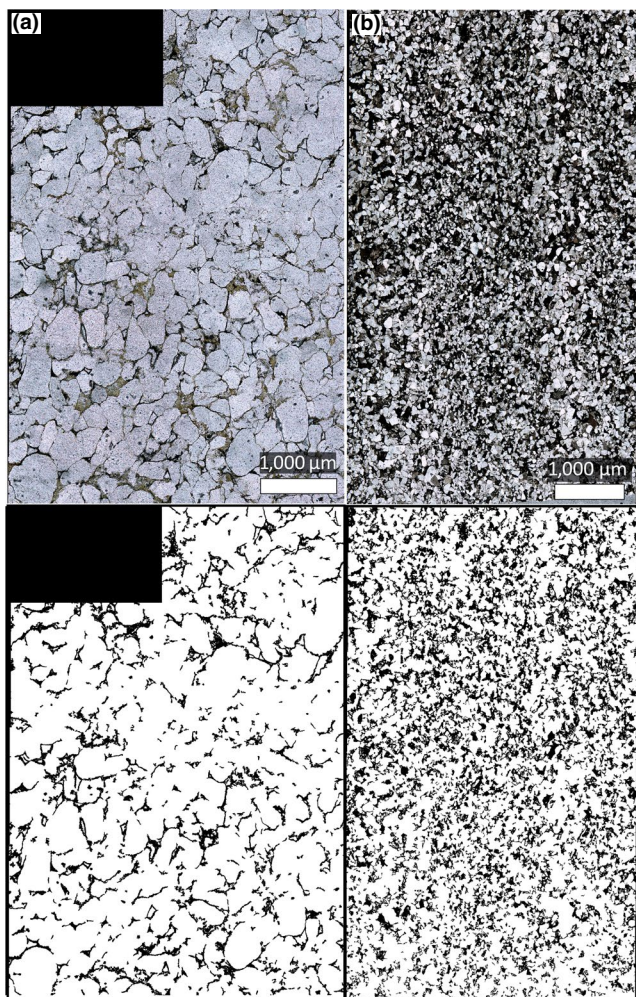
FIGURE 1 Examples of interstitial space images used in this study (full list of images shown in Figures S1 and S2). The images are mosaics reconstituted from several individual images taken with an optical microscope in plane-polarized mode. (a) Mosaic image taken on a medium-grained sandstone containing quartz clasts and minor intercalated mica flakes, with a dark ferruginous cement. (b) Mosaic image taken on a medium-grained sandstone containing subangular quartz and feldspar clasts, with a dark ferruginous cement. The corresponding binarized images, obtained by treatment and segmentation, are shown below

scarce gastropod bioclasts. The bioclasts are strongly abraded and rounded, and do not retain their initial biologic shape. A sparitic cement fills the interstitial spaces between the grains, and fractures within clasts are filled with a similar calcitic cement. In plane-polarized light, the clasts typically appear darker than the cemented pores and fractures, which are easily identifiable.

2.1.2 | System 2: Silica–carbonate biomorphs

This system is represented by 11 images of silica–carbonate biomorphs grown in gel and in solution (Figures S3 and S4). Here,

silica–carbonate biomorphs were grown using laboratory chemicals. However, it has recently been demonstrated that they can grow in modern natural spring waters (García-Ruiz, Nakouzi, Kotopoulou, Tamborrino, & Steinbock, 2017).

In silica gel, silica–carbonate biomorphs form over a few days to several weeks, upon diffusion of a concentrated barium solution (solutions of [Ba] = 0.5 and 1 M here) through an alkaline silica gel in the presence of carbonate ions (Melero-García, Santisteban-Bailón, & García-Ruiz, 2009). They display a crystallization gradient along the direction of diffusion. A total of 10 images of gel-grown biomorphs, which were synthetized in the context of a previous study (Rouillard et al., 2018), were used here (Figure 2; Figures S3 and S4A,B,D,E). Images were taken with an optical microscope using plane-polarized light, at different distances from the diffusion boundary, therefore representing different regimes of growth (Melero-García et al., 2009).

In a silica-rich alkaline solution, silica–carbonate biomorphs form within a few hours upon addition of barium (a [Ba] = 10 mM was used here) and carbonate (being supplied by diffusion of atmospheric CO_2). Solution-grown biomorphs are represented by one image (Figure S4C), synthetized in the context of a previous study (Rouillard et al., 2018). The image was taken with an optical microscope using plane-polarized light.

2.1.3 | System 3: Microbial communities

This system is represented by 10 images of a single strain of cyanobacteria and of a natural microbial community (Figure S5 and S6).

Single-strain bacteria culture: One image was taken on a culture of coccoid cyanobacteria grown in the laboratory (Figure 3a; Figure S5E). This culture consists of a strain of *Synechocystis* sp. from the Pasteur Cyanobacteria Collection (PCC6803) grown with standard BG-11 medium to a stationary growth phase. The image was taken using an optical microscope with contrast enhanced using differential interference contrast (DIC) optics.

Stromatolite-dwelling composite microbial communities: nine images (Figure 3b; Figures S5A–D and S6) were taken in the context of an earlier study (Gérard et al., 2013) on natural mat-forming microbial communities dwelling in carbonate stromatolites in the alkaline crater lake of Alchichica (Cuenca Oriental, Mexico). Fragments of microbial mats were retrieved and imaged using a Confocal Laser Scanning Microscope (Olympus FluoView FV1000) with excitation wavelengths of 405, 488, and 543 nm; the fluorescence image was collected at wavelengths between 425–475, 500–530, and 560–660 nm. No staining was used; the colors in the images represent the autofluorescence of photosynthetic micro-organisms. The images used for the present study contain predominantly unicellular cyanobacteria (pleurocapsales, *Pleurocapsa* sp.), filamentous cyanobacteria (Oscillatoriaceae, *Leptolyngbya* sp.), and potentially some diatoms. During this treatment, the microbial mat underwent little structural deformation, and the images are considered a close morphological match to the natural community.

FIGURE 2 Examples of biomorph images used in this study (full list of images shown in Figures S3 and S4). Silica-witherite biomorphs shown here were grown by diffusion in gels (method described in detail in Melero-García et al., 2009). (b) is taken further away from the diffusion source than (a). Images were taken using an optical microscope in plane-polarized mode; a stack of ~30 images taken along the depth were processed to reconstruct these images. The corresponding binarized images, obtained by treatment and segmentation, are shown below
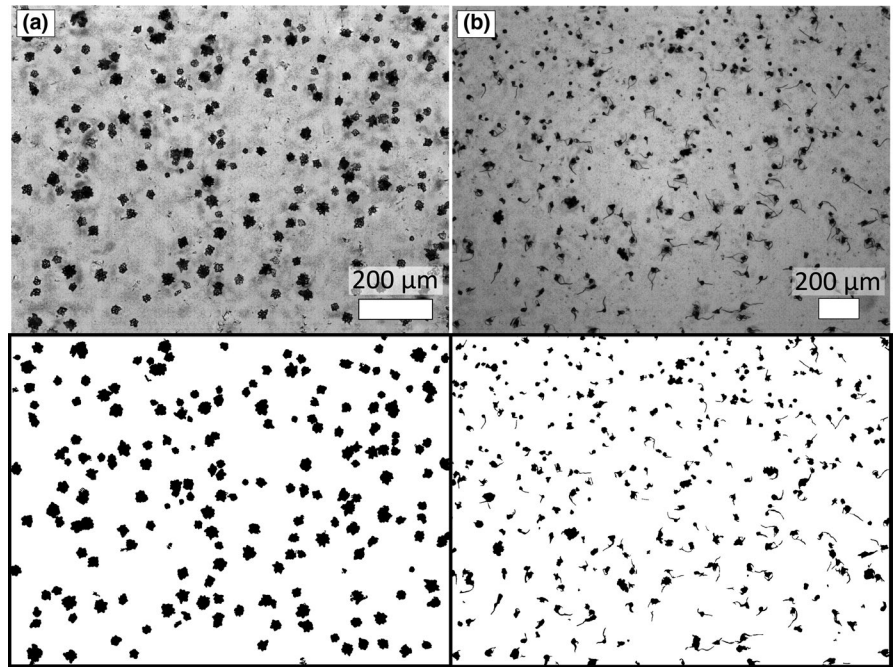
FIGURE 3 Examples of images of microbial populations/communities used in this study (full list of images shown in Figures S5 and S6). (a) Single-strain *Synechocystis* sp. population grown in laboratory and imaged during the stationary phase. (b) Stromatolite-dwelling microbial community from Alchichica crater Lake (Mexico; Gérard et al., 2013). (a) Was taken using an optical microscope with differential interference contrast optics, and (b) was taken using a Confocal Microscope. Colors in (b) are due to the natural autofluorescence of the bacteria (photosynthetic pigments). The corresponding binarized images, obtained by treatment and segmentation, are shown below
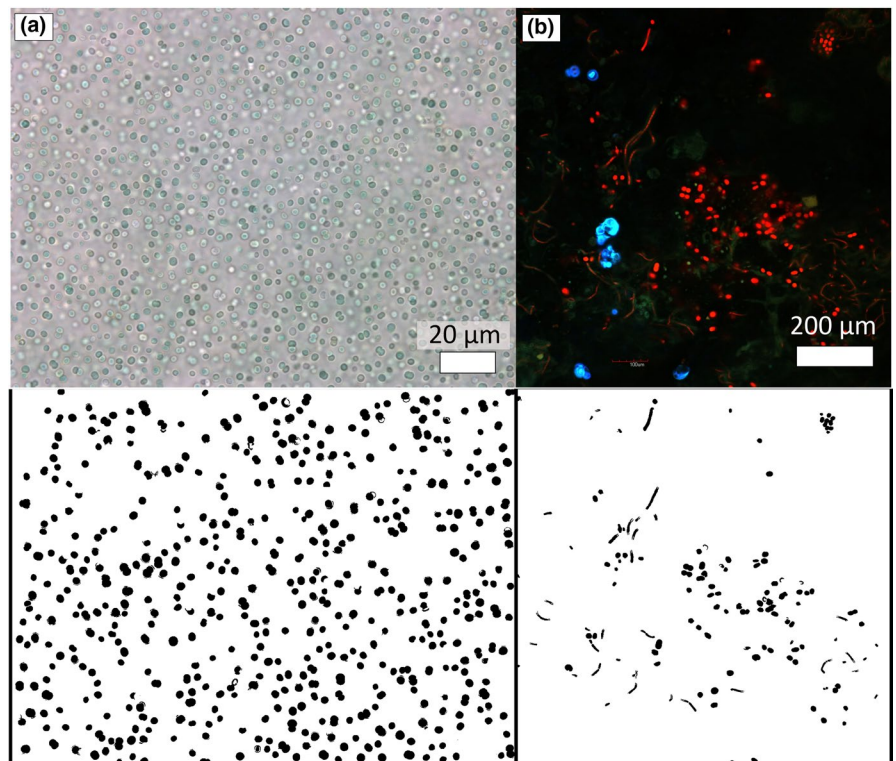
2.1.4 | Test case: Proterozoic Microfossil assemblage

A well-preserved microfossil assemblage from the 1.0 Ga Angmaat Formation (Baffin Island, Canada) was used here as a test. The Angmaat Formation represents deposition in a peritidal, episodically restricted microbial flat with diverse, well-documented fossil microbial mats preserved in early diagenetic chert. Communities commonly contain both filamentous and coccoidal microfossils

(Hofmann & Jackson, 1991; Kah & Knoll, 1996; Kah, Sherman, Narbonne, Knoll, & Kaufman, 1999; Knoll, Worndle, & Kah, 2013; Manning-Berg, Wood, Williford, Czaja, & Kah, 2019). The thin sections used in the context of this study contain an assemblage of coccoidal taxa (*Eogloeocapsa* sp, *Myxococcoides* sp., *Eoentophysalis* sp., *Gloeodiniopsis* sp. and *Polybessurus* sp.). Two specific microfossil-rich areas were imaged in these thin sections (image mosaics are shown in Figure 4a and Figure S7). In order to test the effect of taphonomic variability (Manning-Berg et al., 2019), a smaller, well-preserved
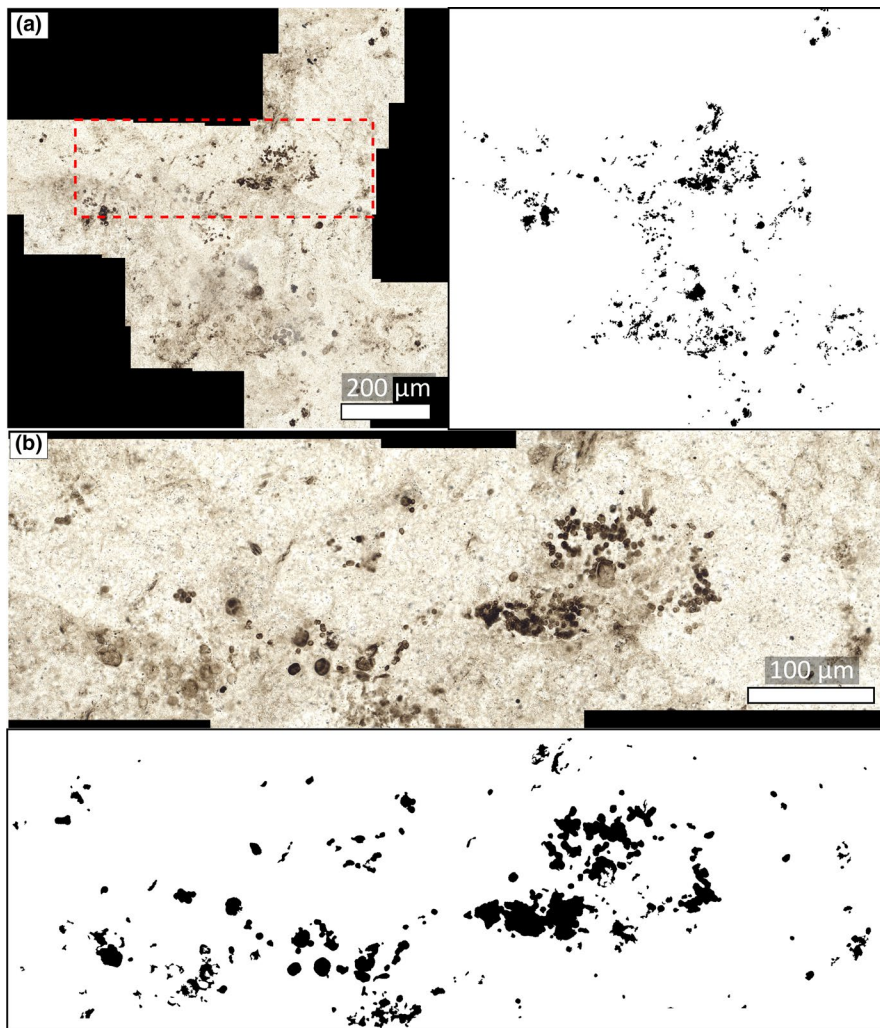
FIGURE 4 (a) Mosaic of a microfossil-rich area in a thin section realized on a chert sample from the 1.0 Ga Angmaat Formation (Baffin Island, Canada). The mosaic was taken using an optical microscope in plane-polarized mode. The red rectangle indicates the region corresponding to (b). Another mosaic is shown in Figure S7. (b) Close-up view of the region outlined in (a). Note the strong degradation of the assemblage in some areas, in which individual microfossils are difficult to segment or even not recognizable anymore. The corresponding binarized images T2 and T2-sub, obtained by treatment and segmentation, are shown on the right of (a) (T2) and below (b) (T2-sub)

area of the mosaic shown in Figure 4a was also used in the study (Figure 4b).

2.2 | Image analysis

All images were treated individually using ImageJ (Abramoff, Magalhaes, & Ram, 2004; Collins, 2007). The images were binarized to separate the populations of microstructures of interest (i.e., interstitial spaces, silica–carbonate biomorphs, and micro-organisms) from their surroundings. For all images, except those corresponding to the two sandstone samples where the cement is difficult to distinguish, the binarization was obtained using the threshold algorithm (the type of threshold was set to "default") of ImageJ. For the images of the two sandstone samples where the interstitial cement is difficult to distinguish from some clasts, the "Trainable Weka Segmentation" plugin was used (Arganda-Carreras et al., 2017). The quality of segmentation for all images in the three systems was substantially improved by applying a size threshold. "Holes" in the particles, which would affect subsequent morphologic measurements, were then removed by artificial filling. Examples of source images with their corresponding treated binarized images are shown for interstitial spaces (Figure 1),

silica–carbonate biomorphs (Figure 2), micro-organisms (Figure 3), as well as for the test case on microfossils (Figure 4). A complete display of all source images and their corresponding binarized images are shown in Figures S1–S6, S8. In the following, microstructures in a binarized image are defined as particles, and all the particles present in one image are defined as a population.

2.2.1 | Characterization of particles in populations

For every particle in an image, the normalized area A (in square pixels) and simple shape descriptors—circularity, C, and solidity, S (dimensionless)—were measured. Circularity is defined as:

$$C = 4\pi A / P^2 \tag{1}$$

where P (in pixels) is the circumference of the particle. This descriptor ranges from 0 to 1, with decreasing values corresponding to increasingly elongated particles (circularity values of example particles are shown in Figure 5a). Solidity is defined as:

$$S = \frac{A}{\alpha} \tag{2}$$

FIGURE 5 Illustration of the key morphologic descriptors used in this paper. (a, b) Circularity and solidity values of some example particles. The particles are ordered with decreasing circularity or solidity values from left to right. The convex hulls (ensemble of straight segments joining the outermost points of the particle) of each particle are drawn in brown in (b). The solidity values decrease when white areas inside the convex hulls are more important. Note that, the two parameters describing different aspects of the shape, the order from left to right is not exactly the same in (a) and (b). (c) Explanation of the measurement of fractal dimension by box-counting method on an example pattern. Grids of boxes with different sizes (ε1, ε2, and ε3) are overlaid on the pattern. The size of boxes represents scale in this method. The number of boxes containing black pixels (green) in the different grids is given as N1, N2, and N3, and represents the amount of detail in this method. A rough estimate of the fractal dimension is first given by a ratio of logs. A better estimate of the fractal dimension is then found using a power-law regression of N versus ε. (d) Lacunarity values of some example patterns. The lacunarity value increases when the overall heterogeneity of the pattern increases
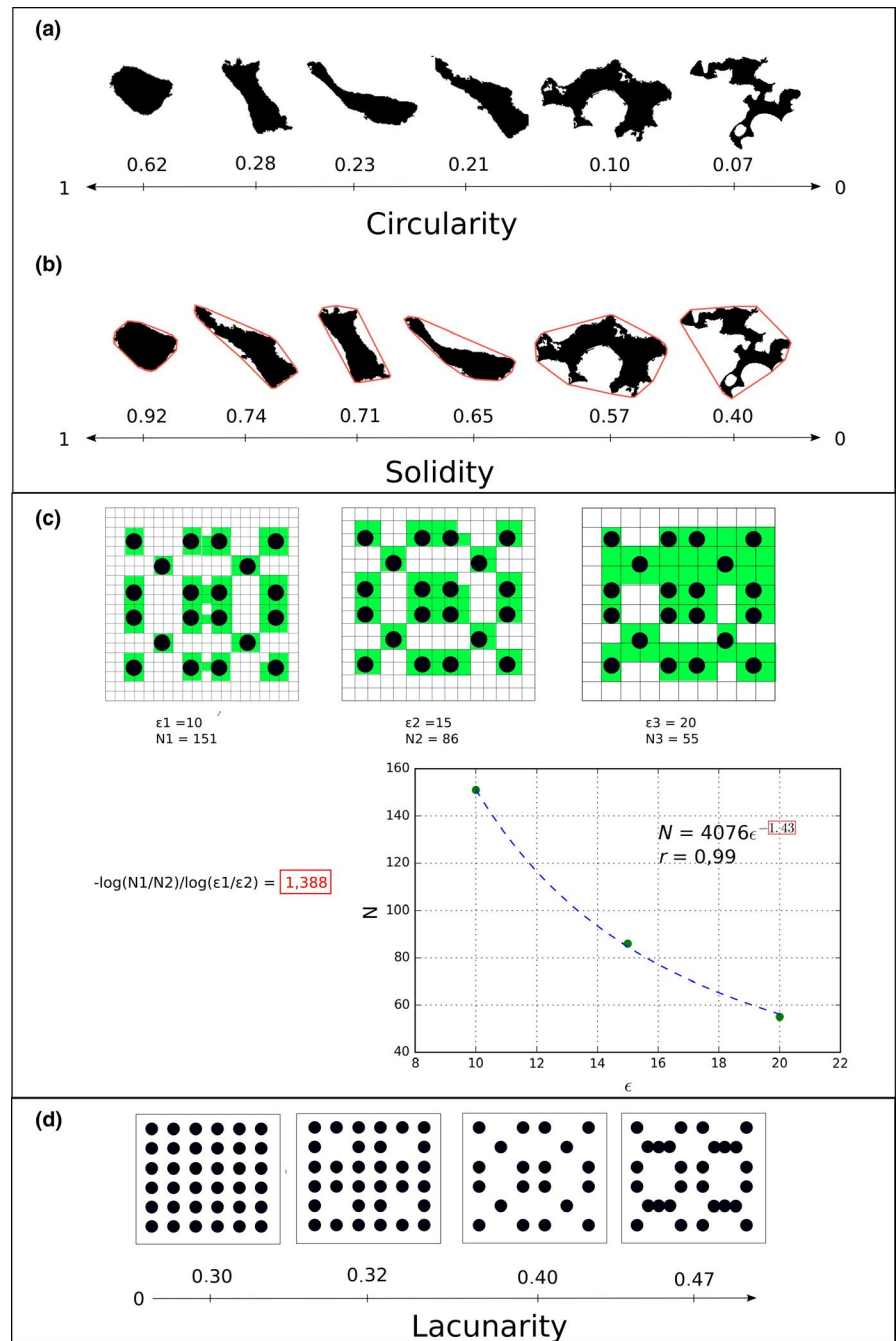
where α is the area (in square pixels) within the convex hull of the particle. The convex hull of a particle is defined by the ensemble of straight segments joining the outermost points of the particle (convex hulls of example particles are drawn in brown on Figure 5b). Solidity ranges therefore from 0 to 1, with higher values representing more convex particles (see Figure 5b). Measurements of circularity and solidity of particles in digital images have been used in various contexts, for example, for quantifying the changes of shape of a fungal strain (*Aspergillus niger*) associated with changes in osmolality in their environment (Wucherpfennig, Hestler, & Krull, 2011), or to characterize the plasticity of cellular nuclei favoring cellular migration in biological tissues (Booth-Gauthier et al., 2013).

2.2.2 | Characterization of populations

In order to describe the overall geometry of populations in the binary images, the parameters of fractal dimension and lacunarity were calculated. A plugin developed for ImageJ (FracLac - Karperien, A., FracLac for ImageJ) was employed.

Generally, the fractal dimension (D, dimensionless) relates detail (N, which may be defined differently depending on the context) with scale (ε, representing a length), by the following relationship:

$$N \propto \varepsilon^{-D} \tag{3}$$

with $\propto$ denoting a proportionality relationship. For 2D objects, D ranges between 1 (fractal dimension of a line) and 2 (fractal dimension of a homogeneous surface). D is commonly estimated via the box-counting method (see Figure 5c for an example of application of this method). In this method, a grid is positioned on the image. The length of box sides in the grid (in pixels) represents the scale, ε, while the amount of detail N at scale ε is estimated by the number of boxes in the grid containing foreground pixels (black pixels here; see green boxes in Figure 5c). This process is repeated several times with different ε values. If N_2 and N_1 are the amount of detail for two different scales ε_2 and ε_1, one can make a rough estimate of the fractal dimension according to the following formula:

$$D = -\frac{\log(N_1/N_2)}{\log(\varepsilon_1/\varepsilon_2)} \tag{4}$$

An example application of Equation (4) is given in Figure 5c. For more couples of values (ε_i, N_i), the change of N with ε is fitted by a power-law regression to obtain a higher quality measurement of fractal dimension D (Figure 5c). The fractal dimension for each image in the three systems was calculated using the box-counting method in FracLac.

Lacunarity quantifies the heterogeneity and the importance of "gaps" in a binary image (see Figure 5d to see how these features relate to the value of lacunarity in example patterns). Using a box-counting method similar to the one used for fractal dimension, the lacunarity λ at a given scale ε can be estimated by

$$\lambda(\varepsilon) = \frac{\sigma(\varepsilon)}{\mu(\varepsilon)} \tag{5}$$

where $\sigma(\varepsilon)$ and $\mu(\varepsilon)$ represent respectively the standard deviation and the average of the pixel count in the boxes of a grid (with boxes of side length ε). For the images of the three systems, a general lacunarity value L was calculated as an average of the λ values found with different ε. The lacunarity value of a homogeneous image is 0, since $\sigma(\varepsilon)$ is equal to 0. There is theoretically no upper limit for the value of lacunarity. For the measure of both D and L, grids of 12 different ε (ranging from 1 pixel to 45% of the image size, with a fixed increment) were used.

2.3 | Statistical analysis

2.3.1 | Description of statistical distributions

Individual distributions were represented graphically as bar histograms. In order to facilitate the comparison between them, the width of the bins is the same in each histogram.

For a parameter X observed in a population of G particles, with a mean $\mu(X)$ and a standard deviation $\sigma(X)$, the shape of the distribution can be described quantitatively (independently of its graphical representation) by three parameters:

The mean divided by standard deviation (Mean/SD), which describes the relative width of the distribution (compare Figure S9A,B):

$$M/SD(X) = \frac{\mu(X)}{\sigma(X)}, \tag{6}$$

skewness, which describes the asymmetry of the distribution (compare Figure S9C,D):

$$S(X) = \frac{1}{G}\sum_{i=1}^{G}\left(X_i - \mu(X)/\sigma(X)\right)^3, \tag{7}$$

and Kurtosis, which describes the importance of tails in the distribution (compare Figure S9E,F):

$$K(X) = \frac{1}{G}\sum_{i=1}^{G}\left(X_i - \mu(X)/\sigma(X)\right)^4. \tag{8}$$

These three parameters were used to quantify the shapes of the distributions of size, circularity, and solidity in all populations.

2.3.2 | Assessment of sampling bias

The qualitative and quantitative descriptions of statistic distributions are subject to error resulting from imperfect sampling of the populations. In order to assess the biases resulting from insufficient sampling, a study of the effect of sampling size was conducted on several test distributions. Size distributions were plotted as bar histograms and characterized quantitatively for different sample sizes. The results are shown in Figure S10 and indicate that the shape of an example distribution (Figure S10A) becomes more variable and potentially less representative of the original population when the sample size decreases (Figure S10B). The relative error made on the descriptors of the tested distributions (Mean/SD, Skewness, Kurtosis) increases exponentially when the sample size decreases (Figure S10C). Although their absolute values may vary, for all distributions tested, the relative errors made on the values of Kurtosis are consistently higher than the relative errors made on the values of skewness and mean/SD. For the current study, large populations were therefore selected when available (median size of populations: 456; range: 87–1,310).

2.3.3 | Parametric correlations between populations

The linear correlation coefficient r between two parameters X and Y, measured on a population of G points, can be calculated according to

$$r(X,Y) = \frac{\sum_{i=1}^{G}(X_i - \mu(X))(Y_i - \mu(Y))}{\sigma(X)\sigma(Y)} \tag{9}$$

The significance of the correlation p (or probability that the two parameters are not correlated) varies with the number of points G and can be calculated with a two-tailed t test according to

$$p(X,Y) = r(X,Y) \sqrt{\frac{G-2}{1-r(X,Y)^2}} \qquad (10)$$

The shape of the statistic distribution of each of the three parameters size, circularity, and solidity was described using the three parameters mean/SD, skewness, and kurtosis. Together they constitute nine parameters describing the distributions in each population. Combined with the two parameters of fractal dimension and lacunarity, a total of 11 parameters are obtained that characterize each population. Linear correlation coefficients r and their associated significances p were calculated between all the couples of these parameters for each system and are given in Tables S1, S2, and S3.

2.3.4 | Discrimination of populations—comparison of different sets of parameters

Multivariate analysis allows the exploration of the combined data from several describing variables (Bishop, Fienberg, & Holland, 2007). Discriminant analysis is a type of multivariate analysis that finds the best linear combinations of variables to maximize the variance between different groups and minimize the variance inside groups. For example, discriminant analysis allows the projection of data on a 2-dimensional slice of the multivariate space for which the groups are optimally separated. Discriminant analysis was used here to maximize the variance between the three different systems: interstitial spaces, silica–carbonate biomorphs, and microbial communities.

Discriminant analyses were performed on populations from the three systems using a variety of parameter sets, that included parameters describing: (a) the distribution of size, (b) the distribution of sizes and general geometric features (fractal dimension, lacunarity), (c) the distributions of shapes (circularity and solidity), (d) the distributions of sizes and shapes, and (e) the combined distributions of sizes, shapes, and general geometric features.

Subsequently, a training analysis was conducted to compare the efficiency of the different sets of parameters to discriminate between systems. The total collection of populations from the three systems (size $N' = 33$) was divided randomly into a training group (size $5 < t < 32$) and a test group (size $N' - t$). The training group was used to run a discriminant analysis. Using the results of this discriminant analysis, a linear classifier assigned each member of the test group to one of the three systems. The efficiency of discrimination is quantified by the rate of correct classification (ρ) achieved by the linear classifier, computed as:

$$\rho = \frac{n(c)}{n(c) + n(u)} \qquad (11)$$

with $n(c)$ being the number of test populations attributed correctly to their system of origin and $n(c) + n(u)$ the total number of test populations. This process was repeated 1,000 times for a given size of the training group. The efficiency of the analysis was assessed by the mean rate of correct classification over these 1,000 repetitions. The different sets of parameters were compared by looking at the evolution of this rate as the size of the training group increased.

3 | RESULTS

3.1 | Characterization of particles in populations

3.1.1 | Size distribution

The size distributions of all populations from the three systems are shown in Figure S11 (in red, interstitial spaces; in blue, silica–carbonate biomorphs; in green, microbial communities). Distributions are plotted as bar histograms, with bins of constant width to facilitate comparison between populations. Representative examples are shown in Figure 6. The parameters describing the size distributions for each population are given in Table 1.

System 1: Interstitial spaces
All populations of interstitial spaces show a similar size distribution: a frequency that decreases monotonically with size, comparable to an exponential or lognormal law (Figure 6a; Figure S11, red histograms). The relative width of the distributions varies quite significantly (average Mean/SD of 0.73, ranging from 0.29 to 1.08; Table 1). Each distribution is strongly positively skewed (average skewness of 8.01, ranging from 2.97 to 20.40; Table 1), and display high to very high positive kurtosis values (average of 119.38, ranging from 12.74 to 520.26; Table 1).

System 2: Silica–carbonate biomorphs
The shapes of the size distributions in the silica–carbonate biomorph populations show only small to moderate variations (Figure 6b,c; Figure S11, blue histograms). Their mean/SD ranges from 2.10 to 4.07, with an average of 3.02 (Table 1). They are positively skewed (average skewness of 0.74, ranging from 0.05 to 1.26—Table 1) and display low to negative kurtosis values (mean kurtosis 1.00, ranging from −0.08 to 2.50—Table 1). Most populations show a simple, unimodal distribution. However, three of the smaller populations display particularly high numbers of particles at the smallest size ranges (Figure 6c; Figure S11b9,b10,b11). This could be due to the insufficient sampling in these populations (Figure S11B).

System 3: Microbial communities
The microbial communities display a wide variety of size distributions. The culture of a single non-colonial cyanobacteria strain (*Synechocystis* sp., Figure 6d) displays a narrow, slightly positively skewed unimodal distribution (mean/SD of 6.30, skewness of 0.72,
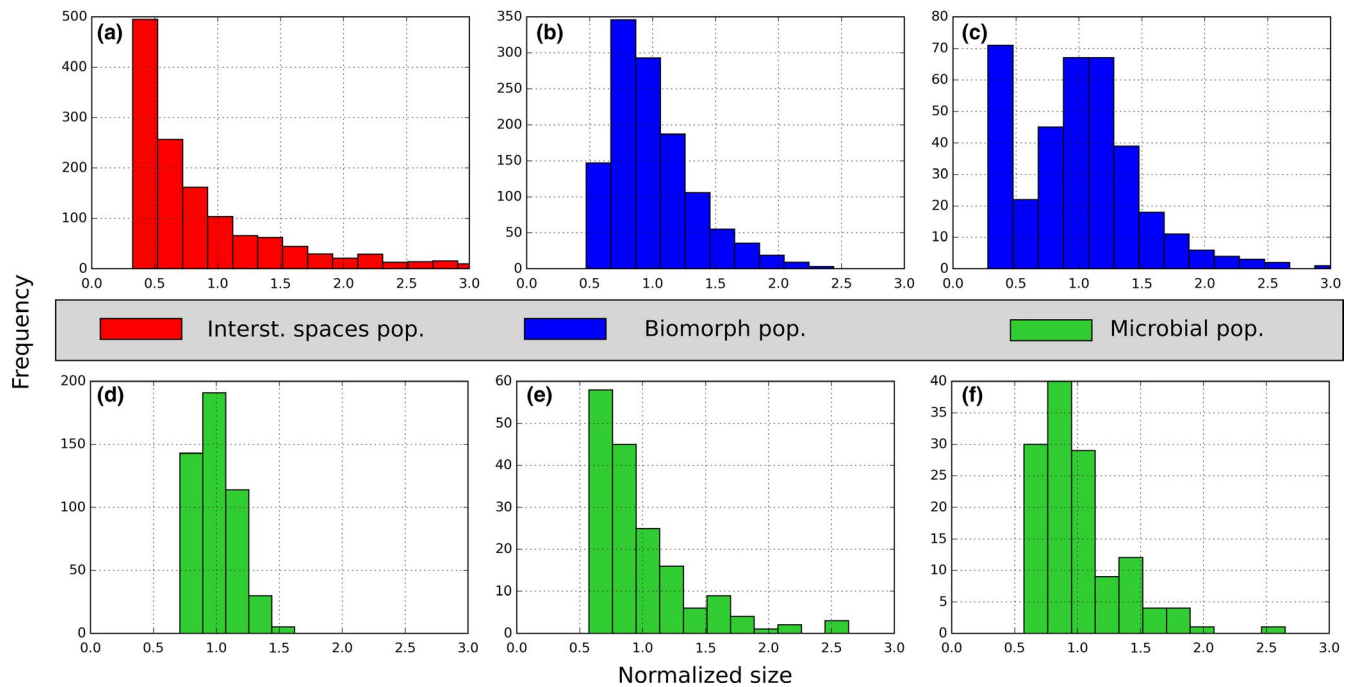
FIGURE 6 Representative distributions of sizes plotted as bar histograms in the three studied systems. The vertical axes represent frequency and the horizontal axes represent size. The sizes are measured as proportional to a radius and normalized to the mean of each distribution. The scale on the x-axis is the same for all populations. In order to facilitate the comparison between histograms, the width of the bins is the same for all studied populations. Red: interstitial spaces populations. Blue: Biomorph populations. Green: Microbial populations

kurtosis of 0.32—Table 1). In contrast, the natural rock-dwelling microbial communities display various shapes of size distributions including unimodal, monotonically decreasing, or multimodal distributions (Figure 6e,f; Figure S11, green histograms). Consequently, the values of mean/SD, skewness, and kurtosis vary significantly between these populations (average Mean/SD of 2.61, ranging from 1.45 to 4.00; average skewness of 2.05, ranging from 1.14 to 2.99; average kurtosis of 7.85, ranging from 2.63 to 18.21—Table 1).

3.1.2 | Relationship between size and shape

Circularity—C—and Solidity—S—(Figure 5a,b) are used here to characterize the variation in particle shape in the populations. For all the studied populations, C and S are plotted against normalized area in Figures S12 and S13, and plots for representative populations are compared in Figure 7. The parameters describing the circularity and solidity distributions for each population are given in Table 1.

System 1: Interstitial spaces
In the system of interstitial spaces, the solidity values decrease with size, converging from a range of 0.6–0.9 at smaller sizes to a range of 0.4–0.6 at larger sizes (Figure 7a, red triangles; Figure S12). The circularity values also decrease markedly with size, converging from a range of 0.2–0.8 at smaller sizes to a range of 0.1–0.3 at larger sizes (Figure 7b, red triangles; Figure S13). Based on these plots, large pores are more concave and elongated than small pores.

System 2: Silica–carbonate biomorphs
For silica–carbonate biomorphs, although the ranges of solidity values vary between populations (0.8–0.9 to 0.4–0.9 depending on the population), the upper values of solidity remain high over the entire range of sizes (Figure 7a, blue diamonds; Figure S12). Conversely, the upper values of circularity steadily decrease with size—from ~1 to ~0.7 when the relative area increases from 0 to 1.5 (Figure 7b, blue diamonds; Figure S13—especially observable on the larger populations).

System 3: Microbial communities
In images of bacterial communities, the circularity/size plots vary significantly between populations (Figure S13), with large ranges of circularity (0.2–1.0). The ranges of solidity are somewhat narrower, ranging from 0.7 to 1.0 (Figure S12). Noticeably, in all these populations, a subpopulation (or the entire population) displays solidity and circularity values independent of size (Figure 7a,b, green circles; Figures S12 and S13), with upper values of circularity and solidity staying at 0.9–1.0 for normalized areas increasing from 0 to 1.0–1.5.

3.2 | Characterization of populations

3.2.1 | Fractal dimension and lacunarity

The results of fractal dimension and lacunarity measurements by box-counting method, describing the overall geometry of the

TABLE 1 Morphologic descriptors of the different populations

System	N	R MSD	C MSD	S MSD	R skew.	C skew.	S skew.	R kurt.	C kurt.	S kurt.	D	L
I	574	0,98	1,97	5,11	3,05	0,48	−0,53	15,27	−0,19	−0,30	1,79	0,44
I	818	0,74	1,76	4,85	4,70	0,79	−0,16	30,31	0,34	−0,53	1,82	0,22
I	946	1,10	2,21	5,84	4,10	0,24	−0,46	24,41	−0,64	−0,29	1,80	0,43
I	398	0,90	2,23	5,73	3,00	0,34	−0,89	10,65	−0,50	0,60	1,73	0,84
I	139	1,65	2,10	5,18	2,28	0,53	−0,51	6,51	0,09	0,03	1,62	0,46
I	259	2,33	1,98	5,32	2,12	0,84	−0,17	5,89	0,32	−0,32	1,68	0,79
I	1,334	1,14	2,05	4,79	4,84	0,36	−0,53	44,52	−0,35	−0,26	1,77	0,31
I	999	0,89	2,08	4,73	6,17	0,33	−0,55	54,96	−0,40	−0,35	1,80	0,31
I	134	0,29	1,83	5,17	9,89	0,53	−0,59	105,83	−0,27	−0,05	1,83	0,24
I	959	0,82	1,98	5,09	4,48	0,49	−0,53	27,39	−0,10	−0,21	1,71	0,42
I	649	0,69	1,83	4,94	6,45	0,61	−0,37	60,65	−0,02	−0,35	1,70	0,41
B	1,202	2,95	3,99	11,74	1,26	−0,67	−1,45	2,50	−0,10	2,59	1,69	0,27
B	1,306	2,89	4,07	13,15	1,11	−0,69	−1,23	1,56	−0,19	1,78	1,71	0,26
B	1,169	2,95	4,87	16,83	0,83	−1,06	−1,53	0,62	0,56	2,64	1,69	0,27
B	173	3,76	4,34	14,40	0,16	−1,06	−2,22	−0,08	0,85	6,19	1,52	0,38
B	356	2,10	1,97	4,10	0,71	0,53	−0,35	1,09	−0,62	−0,81	1,48	0,51
B	333	2,47	1,83	4,28	0,73	0,66	−0,47	0,99	−0,66	−0,45	1,53	0,37
B	819	3,51	4,42	12,75	0,92	−0,61	−1,16	0,46	−0,13	1,46	1,64	0,28
B	122	4,07	3,79	12,00	0,82	−0,42	−0,65	0,39	0,29	0,16	1,44	0,42
B	1,215	3,05	5,19	17,25	0,98	−1,03	−1,57	0,91	0,81	3,12	1,69	0,26
B	192	3,06	3,60	12,85	0,59	−0,61	−1,83	2,38	0,38	5,77	1,52	0,39
B	133	2,48	3,11	10,26	0,05	−0,67	−1,73	0,21	−0,77	3,00	1,47	0,57
M	127	3,09	2,44	6,97	1,14	−0,61	−1,57	2,63	−1,19	2,35	1,20	0,99
M	188	2,49	2,32	5,02	2,34	−0,32	−1,24	7,43	−1,16	0,80	1,31	1,09
M	170	2,34	2,21	5,14	2,17	−0,05	−0,94	6,04	−1,11	0,22	1,49	0,67
M	130	2,94	2,54	6,77	1,69	−0,13	−0,87	4,10	−1,06	0,40	1,56	0,55
M	237	1,62	2,75	6,45	2,72	−0,43	−1,44	14,94	−0,62	2,10	1,69	0,45
M	153	1,45	2,39	5,27	2,99	−0,49	−1,58	18,21	−1,05	2,45	1,51	0,68
M	87	2,35	3,54	8,38	2,44	−1,18	−2,75	9,33	1,16	9,69	1,39	0,63
M	430	4,00	3,19	7,24	1,37	−0,81	−1,92	3,84	−0,24	3,88	1,49	0,67
M	229	3,18	4,01	9,88	1,62	−1,20	−2,65	4,14	1,02	8,16	1,39	0,76
M(PCC)	483	6,30	3,94	18,96	0,72	−1,15	−2,81	0,32	0,22	9,96	1,63	0,29

Note: Each row in the table represents a single population. System: system of origin of the population (I: interstitial spaces, B: biomorphs, M: microbes) – *Nota Bene*: M(PCC) designates the cultured population of *Synechocystis* sp. All the descriptors are adimensional. *N*: number of particles in the population. MSD: Mean/*SD* of statistic distributions. skew.: skewness of statistic distributions. kurt: kurtosis of statistic distributions. R: distribution of sizes (equivalent radius) in the population. C: distribution of circularities in the population. S: distribution of solidities in the population. D: fractal dimension. L: lacunarity.

different populations from the three systems, are given in Table 1 and are represented in Figure 8a. Microbial communities have a wide range of fractal dimensions (1.2–1.7) and lacunarity (0.3–1.1). In contrast, populations of interstitial spaces and silica–carbonate biomorphs have a narrower range of fractal dimensions (1.4–1.7 for biomorphs, 1.7–1.8 for interstitial spaces) and lacunarity values (0.2–0.6 for biomorphs, 0.2–0.5 for interstitial spaces—apart from one outlier population). Microbial communities and silica–carbonate biomorph populations exhibit a similar negative correlation between the two parameters.

3.2.2 | Parametric correlations between populations

Three dimensionless parameters that describe the shape of distributions (mean/*SD*, skewness, and kurtosis) were determined for size distributions, but also for circularity and solidity distributions. Every population can consequently be described by these nine parameters, and by fractal dimension and lacunarity (11 parameters in total—Table 1). The three systems may be distinguished by distinct ranges for some of these parameters (e.g., in Figure 8b,c). For example, the different populations of interstitial spaces display a large
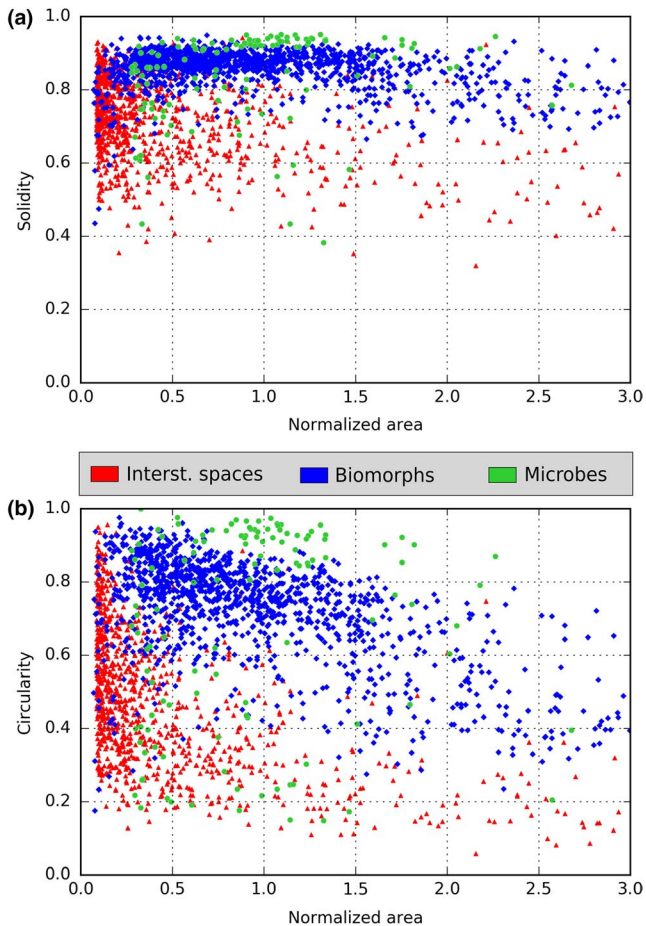
(a)

(b)

Interst. spaces   Biomorphs   Microbes

FIGURE 7 Comparison of the relationship between area (normalized to the mean of the distribution) and shape in the three systems. (a) Solidity of three example populations (derived from the different systems) as function of their area. (b) Circularity in the same populations as function of their area. Red triangles: interstitial spaces in an oolitic limestone. Blue diamonds: biomorphs grown in gel. Green circles: bacteria in a fragment of mat from Lake Alchichica, Cuenca Oriental, Mexico

range of kurtosis values for their size distributions (12.74–520.26), whereas silica–carbonate biomorph populations display a much narrower range (−0.08 to 2.50)—Figure 8c. Conversely, the different populations of biomorphs have very different values of kurtosis for their solidity distributions (−0.81 to 6.19), whereas the different populations of interstitial spaces display a much narrower range of values (−0.65 to 0.10)—Figure 8c. In each system considered separately, the correlation coefficients between these 11 parameters were calculated for every couple of parameters and are given in Tables S1, S2, and S3. The correlation coefficients (r) are shown in the lower left part of these tables, and the associated probabilities of non-correlation (p) are shown in the upper right part of these tables. Some pairwise correlations point out critical differences distinguishing the microbial communities from the two other systems. Examples of such differences are plotted in Figure 8d–f. The skewness of the size distributions in microbial communities is negatively correlated to the mean/SD (Figure 8d, green—$r = −.89$, $p = .0006$).

On the contrary, silica–carbonate biomorph populations do not display a correlation between the mean/SD and the skewness of their size distributions (Figure 8d, blue – $r = .02$, $p = .95$). It is also observed that the kurtosis of the circularity distributions in microbial populations is negatively correlated to the skewness of this distribution (Figure 8e, green—$r = −.89$, $p = .0005$) and to the skewness of the solidity distribution (Figure 8f, green—$r = −.90$, $p = .0004$), whereas opposite correlations are observed for populations of interstitial spaces (Figure 8e,f, red—respectively $r = .97$, $p = 1E-6$, and $r = .83$, $p = .002$).

3.2.3 | Discrimination of populations—comparison of different sets of parameters

A quantitative study using discriminant analysis was made to test if populations from the three systems could be efficiently differentiated. This was done for the following five sets of parameters:

Set 1: Mean/SD, skewness and kurtosis of the size distributions (three parameters).

Set 2: Mean/SD, skewness and kurtosis of the size distributions, fractal dimension, lacunarity (five parameters).

Set 3: Mean/SD, skewness and kurtosis of the circularity and solidity distributions (six parameters).

Set 4: Mean/SD, skewness and kurtosis of the size, circularity and solidity distributions (nine parameters).

Set 5: Mean/SD, skewness and kurtosis of the size, circularity and solidity distributions, fractal dimension and lacunarity (11 parameters).

Results of discriminant analyses performed with all the populations and with the five different sets are shown in Figure 9a–e. As mentioned earlier, the axes on the 2D plots represent the linear combinations of all considered parameters that maximize the variance between the three systems (on a 2D plane). The efficiency of discrimination as a function of the number of considered populations is plotted on Figure 9f (the curves obtained for the different sets of parameters are also shown on distinct plots in Figure S14).

The results of the discriminant analyses run with the different sets of parameters are as follows:

1. A discriminant analysis run with Set 1 on all populations shows the microbial populations very close from the two other systems (Figure 9a). When the number of populations considered in the discriminant analyses increases, the rate of correct classification reaches a plateau for a small number of populations (about 12 populations), then raises slowly above 20 populations to reach ~80% of correct classification (Figure 9f, hollow circles).
2. A discriminant analysis run with Set 2 on all populations shows that the three systems are contiguous, with a slight overlap between the microbial populations and silica–carbonate biomorph populations (Figure 9b). When the number of populations considered in the discriminant analyses increases, the rate of correct classification increases faster than for the other sets up to ~15

populations, and levels off then to reach 85% (Figure 9f, light gray pentagons).

3. A discriminant analysis run with Set 3 on all populations shows again that the biomorph populations overlap with microbial

populations (Figure 9c). When the number of populations considered in the discriminant analyses increases, the rate of correct classification follows a trend very close to that observed for Set 2 (Figure 9f, gray stars).
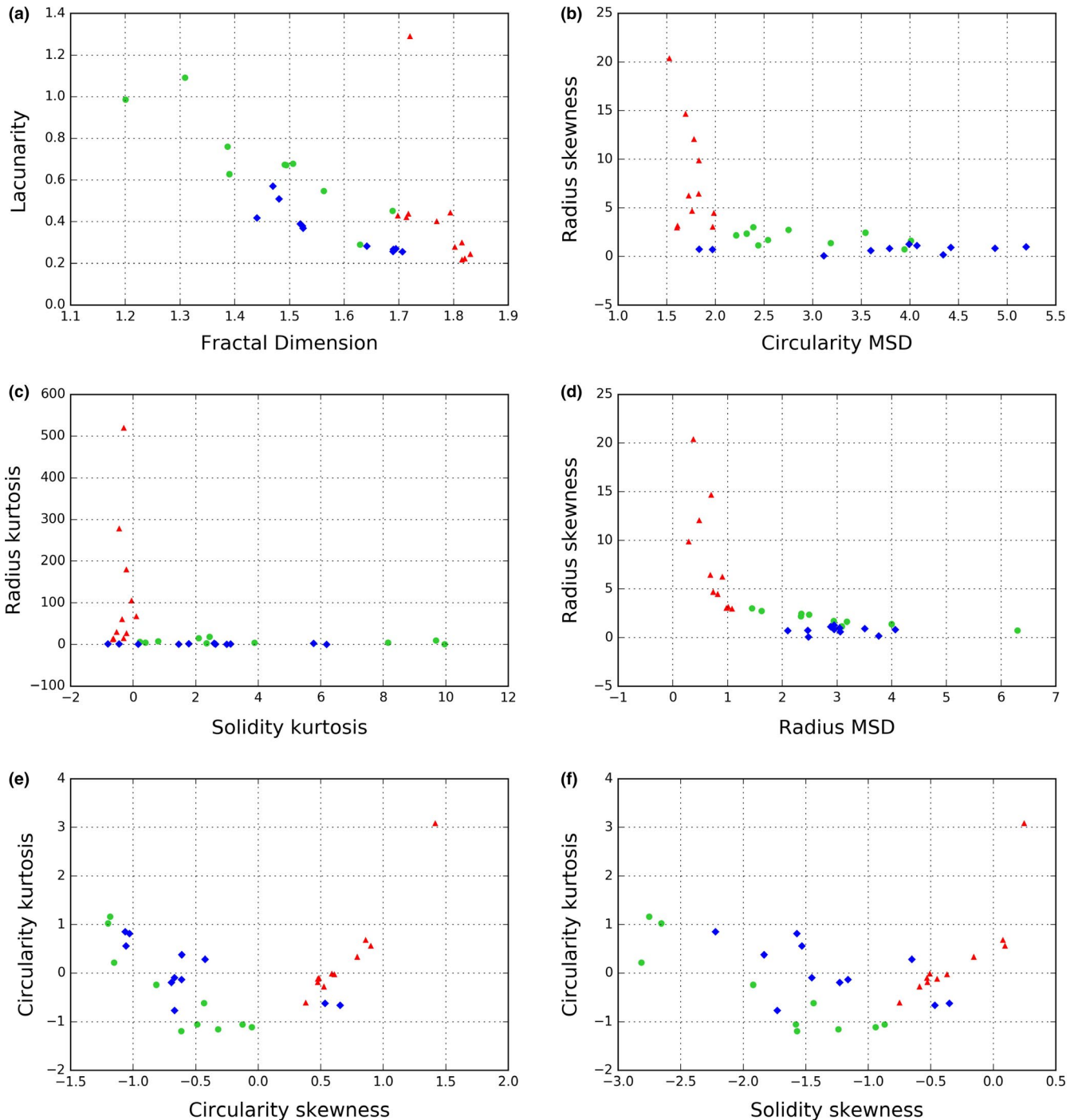

FIGURE 8 Plots of pairs of population-describing parameters allowing to discriminate the different systems. (a) Fractal dimension plotted against Lacunarity in all images from the three systems. (b) Mean/*SD* of the circularity distributions plotted against the skewness of the size distributions in all populations from the three systems. (c) Kurtosis of the solidity distributions plotted against the kurtosis of the size distributions. (d) Mean/*SD* of the size distributions plotted against the skewness of the size distributions. (e) Skewness of the circularity distributions plotted against the kurtosis of the circularity distributions. (f) Skewness of the solidity distributions plotted against the kurtosis of the circularity distributions. Red triangles: interstitial spaces populations. Blue diamonds: biomorph populations. Green circles: Microbial communities. Correlation coefficients (Linear *r* of Pearson) and associated probabilities of non-correlation (*p*) are given for all pairs of parameters in Table S1
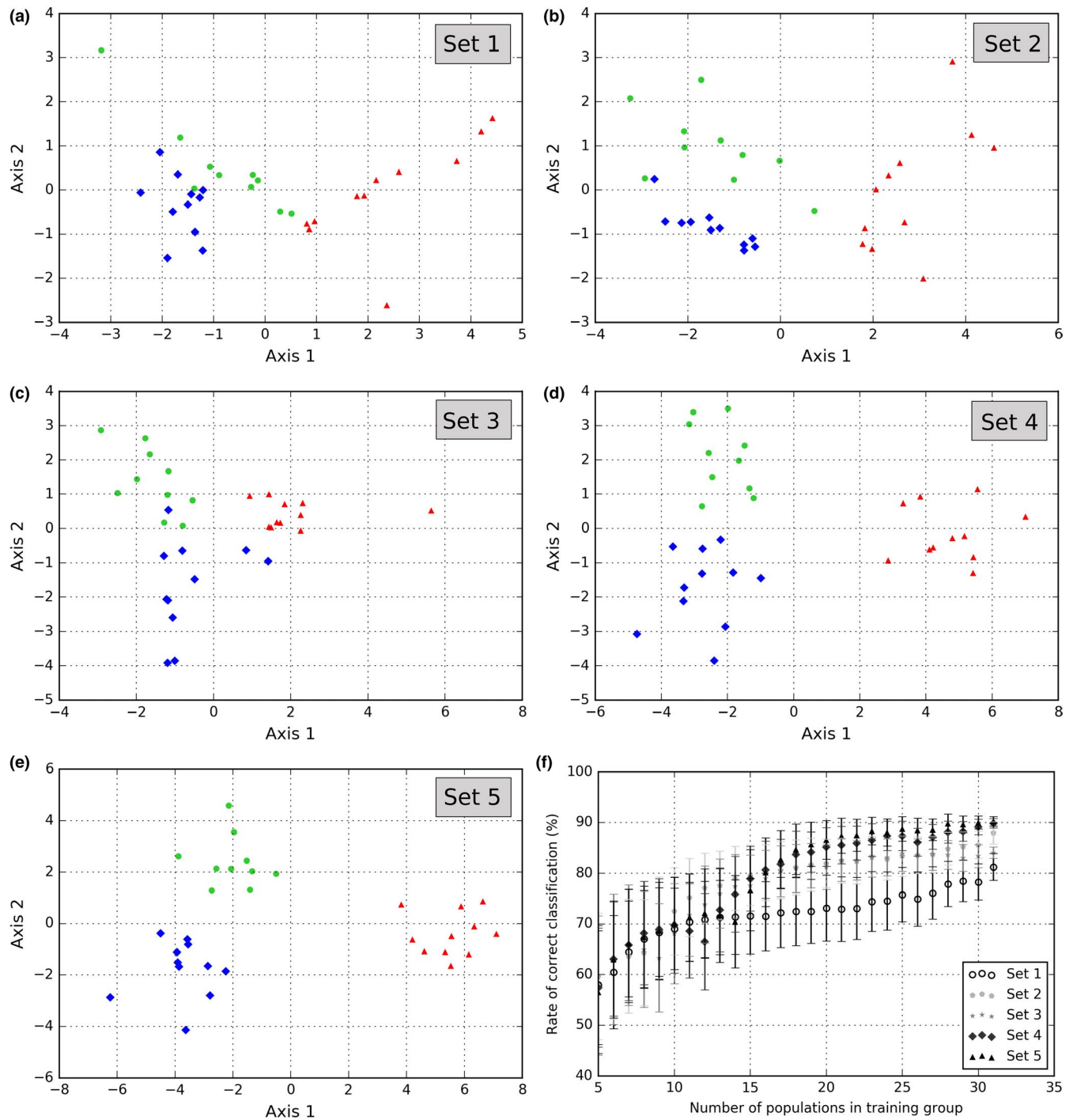
FIGURE 9 Comparison of the efficiency of the discrimination achieved by different sets of parameters. The axes correspond to linear combinations of all parameters in the considered set that allow to maximize the variance between the different systems in a 2D-space (Axis 2 vs. Axis 1). Discriminant analyses were run with all populations from the three systems. The following combinations of parameters (sets) are shown. (a) Set 1: Mean/*SD*, skewness and kurtosis of size distribution. (b) Set 2: Mean/*SD*, skewness and kurtosis of size distribution, fractal dimension and lacunarity. (c) Set 3: Mean/*SD*, skewness and kurtosis of circularity and solidity distributions. (d) Set 4: Mean/*SD*, skewness and kurtosis of size, circularity and solidity distributions. (e) Set 5: Mean/*SD*, skewness and kurtosis of size, circularity and solidity distributions, fractal dimension and lacunarity. Red triangles: Interstitial spaces population. Blue diamonds: Biomorph populations. Green circles: Microbial populations. (f) Evolution of the rate of correct classification of populations to the three systems with the number of populations in the training group, using the different sets of parameters previously described. Error bars represent 2 *SD* obtained on 1,000 iterations for a single size of training group. Hollow circles: Classification with discriminant analyses using the parameters of Set 1. Light gray pentagons: Classification with discriminant analyses using Set 2. Gray stars: Classification with discriminant analyses using Set 3. Dark gray diamonds: Classification with discriminant analyses using Set 4. Black triangles: Classification with discriminant analyses using Set 5

4. A discriminant analysis run with Set 4 on all populations separates the three systems (Figure 9d). The rate of correct classification increases steadily up to 19–20 populations considered in the analyses, with ~85% of correct classification (Figure 9f, dark gray diamonds). The curve is then leveling off, reaching 90% of correct classification with 31 populations in the discriminant analysis.

5. A discriminant analysis run with Set 5 on all populations separates the three systems even more efficiently than Set 4 (Figure 9e). When the number of populations considered in the discriminant analyses increases, the rate of correct classification follows a trend almost identical to that identified on Set 4 (Figure 9f, black triangles).

3.3 | Test case: microfossil populations from the 1.0 Ga Angmaat Formation

3.3.1 | Size distribution

In the three images from the Angmaat Formation, distributions show a monotonically decreasing size trend (Figure 10b; Figure S15) similar to the size distributions of interstitial spaces, but somewhat narrower (Mean/SD ranging between 1.01 and 1.48).

3.3.2 | Relationship between size and shape

Similar to silica–carbonate biomorphs and micro-organisms, solidities are high (0.6–1.0) and independent of particle size (Figure 10a, black squares and hollow stars; Figure S15). The evolution of circularities with size is, overall, similar to that observed for interstitial spaces (Figure S15). However, similar to observations of modern microbial communities, circularity values remain high at small sizes (below 0.5 in normalized area).

3.3.3 | Parametric correlations between populations

On diagrams plotting population-describing parameters, parameters describing size distributions appear unable to attribute fossil microbial assemblages of the Angmaat Formation to one of the three systems (e.g., see skewness of size distributions in Figure 10d). However, the parameters describing shape distributions show clearly that populations of the Angmaat Formation can be split into two groups. The two large mosaics T1 and T2 have circularity and solidity distributions similar to interstitial spaces and may even show the same correlations (Figure 10e). T2-sub, which represents only a part of T2, has circularity and solidity distributions similar to microbial communities (Figure 10d,e).

3.3.4 | Discrimination of populations

In discriminant analyses, microfossil assemblages of the Angmaat Formation are not systematically attributed to one of the three

systems (Figure S15J–L). For example, in a discriminant analysis using the Set 5 of parameters (size and shape distributions, plus fractal dimension and lacunarity—Figure S15L), the three populations (T1, T2, and T2-sub) plot between the three systems.

4 | DISCUSSION

4.1 | Discrimination—from individuals to entire populations

4.1.1 | Size distribution

In the system of interstitial space populations, all parameter measurements display a monotonously decreasing distribution within the population (Figure 6a; Figure S11). These results are comparable to the lognormal or power-law distributions found in previous measurements of interstitial spaces in clastic sedimentary rocks (Crisp & Williams, 1971; Curtis, Sondergeld, Ambrose, & Rai, 2012; Diamond, 1970; Fusseis et al., 2012; Kuila & Prasad, 2013; Loucks, Reed, Ruppel, & Jarvie, 2009). It is also consistent with results obtained in a study on hydrodynamic modeling of the pore structure of sandstones (Ioannidis & Chatzis, 1993). Since a broad variety of sandstones, as well as one limestone, was selected for this study, it can be inferred that the nature of their clasts or their packing characteristics do not significantly affect the overall shape of the size distributions.

In the system of silica–carbonate biomorphs, a unimodal, positively skewed size distribution is typically observed (Figure 6b; Figure S11), confirming the results of a previous study of Rouillard et al. (2018). Size distributions of crystals grown experimentally or observed in nature can be explained and modeled by specific regimes of nucleation and growth (Eberl, Drits, & Srodon, 1998; Kile, Eberl, Hoch, & Reddy, 2000). According to these studies, the size distributions observed here for biomorphs correspond to a nucleation with decaying rate followed by surface-controlled growth. The decaying rate of nucleation is consistent with the gel environment used here for growing silica–carbonate biomorphs; the diffusion of barium is slow in this medium and their supply is limited (Eberl et al., 1998; Kile et al., 2000). The surface-controlled growth is also consistent with previous measurements that the growth rate of silica–carbonate biomorphs varies linearly with time (Zhang, 2015). However, silica–carbonate biomorphs are aggregates rather than single crystals, and the pH—and therefore saturation state of the growth medium—oscillates locally during biomorph growth (Montalti et al., 2017). As a consequence, silica–carbonate biomorph size distributions are not readily described by the same processes which explain the growth of single crystals. Overall, the size distribution of biomorphs is consistently distinct from the size distribution of interstitial spaces.

In the system of micro-organism populations, the single-strain, non-colonial population displays a unimodal size distribution clearly distinct from that of interstitial spaces populations and narrower than that of silica–carbonate biomorph populations
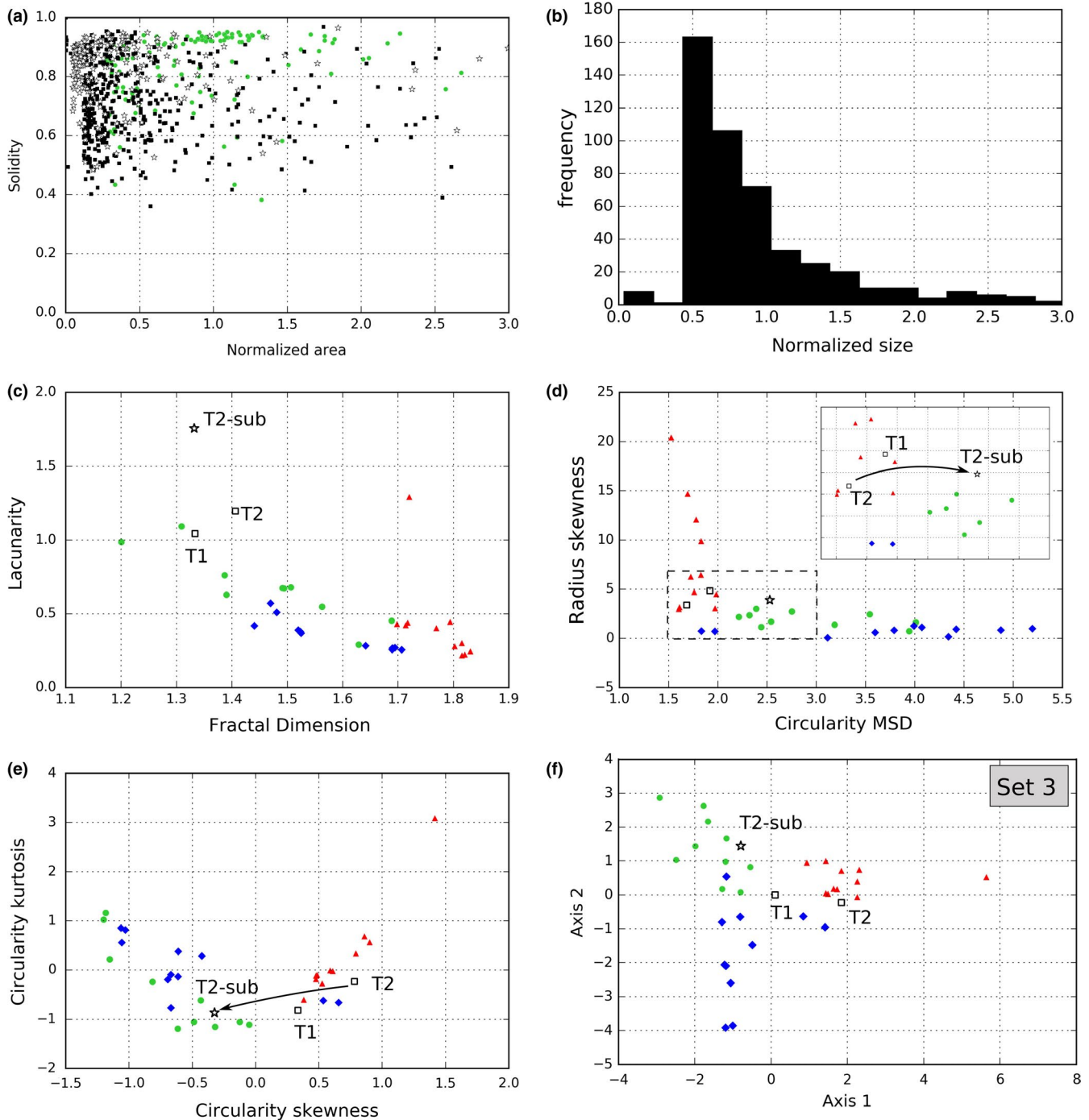
FIGURE 10 Application of the analytic protocol to microfossil assemblages from the Angmaat formation (1.0 Ga, Baffin Island, Canada). (a) Evolution of the solidity of the particles with their size in T2 (cf. Figure 4a; black squares in Figure 10a) and in a subset of T2, T2-sub (cf. Figure 4b; hollow stars in Figure 10a) compared to a microbial community. (b) Size distribution in T2. (c, d, e) Comparison of the Angmaat populations with the three different systems in some plots of pairs of population-describing parameters shown in Figure 8. The two large images (T1 and T2, Figure 4a; Figures S7 and S8) are shown as hollow squares, the subset of T2 (Figure 4b) is shown as a hollow star. (c) Fractal dimension plotted against lacunarity. (d) Mean/*SD* of the circularity distribution plotted against the skewness of the size distribution. A close-up view of the area outlined by the black dotted frame is shown in the upper right part of the plot. (e) Skewness of the circularity distribution plotted against the kurtosis of the circularity distribution. (f) Location of the Angmaat populations on the morphospace obtained with a discriminant analysis run on all populations from the three systems using the set 3 (descriptors of solidity and circularity distributions)

(Figure 6d; Figure S11m10; line PCC in Table 1). This kind of distribution has been reported and modeled in previous studies (Harvey & Marr, 1966; Katz et al., 2003; Koch, 1966; Uysal, 2001). On the other hand, the size of colonial, filamentous strains is not only controlled by the growth of individual bacteria, but also by the number of cellular divisions; the resulting size distributions may

resemble that of interstitial spaces (Figure 6e; Figure S11m2,m3). Natural microbial communities are often composed of different colonial and non-colonial strains, each with a different size distribution. Depending on the nature of the strains and their relative abundances, these communities exhibit therefore more complex and various size distributions. Given this complexity of natural microbial communities, a distinction from the two other systems can potentially be made using their multimodal size distribution (Figure 6f; Figure S11m1,m4,m7,m8). This approach does not work, however, if the different strains constituting the community have similar sizes; in these cases, the multimodal character of the distribution may remain undetected. For example, the distribution shown in Figure S11m6, which resembles a unimodal biomorph distribution, was measured on a complex community and probably hides an underlying multimodal distribution. Overall, single, non-colonial strains of micro-organisms and many complex communities can be distinguished from abiogenic populations by qualitative comparison of their size distribution. Nevertheless, in some complex communities, multimodal distribution is difficult to prove and may only be confidently detected with highly resolved histograms (obtained on large populations). Size distributions should therefore be used with caution for studies on biogenicity. Prior hypotheses about the type of population (e.g., colonial or not) should be made before their interpretation. One potential solution to overcome these issues may be to look at the variability of size distributions within a sample (see further, Section 4.1.4).

4.1.2 | Relationship between size and shape

In the system of interstitial space populations, a clear trend is seen in the relationship between size and shape. The solidity (Figure 7a) and circularity (Figure 7b) of interstitial spaces appear to decrease with their size. In other words, their shapes become more complex as their size increases. We make the hypothesis that this phenomenon is due to the constraining of the shape of interstitial spaces by their surrounding mineral matrix.

In the system of silica–carbonate biomorphs (gel-grown populations and solution-grown population), the solidity appears to be nearly independent of size (Figure 7a), while circularity decreases with size (Figure 7b). This decrease in circularity with size is less pronounced than that observed for interstitial spaces.

In the system of microbial communities, by contrast, it appears that solidity (Figure 7a) and circularity (Figure 7b) are independent of size. This may be ascribed to the presence of non-colonial strains. Indeed, the shape of an individual cell is regulated through complex intracellular mechanisms (Ausmees, Kuhn, & Jacobs-Wagner, 2003; Ingber, 2003; Jones, Carballido-López, & Errington, 2001; Pinho, Kjos, & Veening, 2013). The relationship between size and shape, as quantified here by circularity and solidity (Figure 7; Figures S12 and S13), has in most cases enabled a distinction between the three systems. This relationship represents therefore an interesting criterion for discriminating non-colonial

biologic populations from certain abiogenic systems such as interstitial spaces and silica–carbonate biomorphic crystal aggregates. This relationship is not systematically verified, however, in communities that are strongly dominated by colonial strains. For these strains, the relationship between shape and size depends first on the modalities of association of cells in the colony. For example, filamentous colonies display more elongated and sinuous shapes when they increase in size; they display therefore similar trends as interstitial spaces. In contrast, some colonies may actually preserve their shape during growth, such as colonies with no preferential orientation during cellular divisions, which preserve spheroidal shapes (e.g., colonial chlorophyceae *Sphaerocystis* sp.—Tsarenko, 2006).

4.1.3 | Fractal dimension and lacunarity

The three systems appear to occupy different areas on the *D–L* plot (Figure 8a). In particular, the populations of silica–carbonate biomorphs and interstitial spaces display distinct couples of *D* and *L* values. In contrast, half of the images of microbial populations display low values of fractal dimension (1.2–1.4) and high values of lacunarity (0.6–1.1), which differ from the two other systems. However, the other images of microbial populations have values of fractal dimension and lacunarity very close to or overlapping with the two abiogenic systems. Fractal dimension and lacunarity seem not to be good indicators of biogenicity in this specific study. It must also be noted that these two parameters are strongly affected by the density (especially for lacunarity) and the dispersion or aggregation (especially for fractal dimension) in populations. As a consequence, larger ranges of values would probably be found for the different systems if they were represented by populations from more diverse sources. More studies are needed to establish whether controls specific to each system exist for these parameters.

4.1.4 | Parametric correlations between populations

The shapes of statistic distributions illustrate underlying processes independent of the absolute size or shape of particles in the populations (see Section 4.1.1 for the example of size distributions). The statistic distributions in microbial populations display large ranges of values for mean/*SD*, skewness, and kurtosis; these values are close to those found in silica–carbonate biomorph populations, but often differ markedly from those found in interstitial space populations (Figure 8b,c). Furthermore, the *variability* of the shape of the distributions appears to be constrained. For example, the mean/*SD* and skewness of size distributions in microbial populations are correlated (Figure 8d): size distributions of microbial populations cannot display any kind of shape (i.e., microbial communities do not occupy the space indiscriminately on Figure 8d, but instead, they are constrained on a line). We hypothesize that this is caused by the limited

number of strains imaged in this microbial mat. According to this hypothesis, the variability of statistic distributions in the microbial populations could be controlled by changes in the relative abundances of the different strains. The control on the variability of the shape of distributions differs in the two other systems (Figure 8d for size distributions, Figure 8e for circularity distributions; Tables S1, S2, and S3). Interestingly, correlations also appear to exist between different types of distributions in the three systems. For example, the shapes of the circularity and solidity distributions seem related—although, here again, the correlation is not the same for interstitial spaces populations and microbial populations (Figure 8f; Tables S1 and S3). Overall, the differences in statistic correlations at the system-level allow microbial populations to be distinguished from the two abiogenic systems in our study and constitute a potential biosignature.

4.1.5 | Discrimination of entire populations—comparison of different sets of parameters

It can be seen in Figure 9f and Figure S14 that the total number of parameters used in the discriminant analyses (increasing from set 1 to set 5) is not the only factor controlling the efficiency of discrimination. Indeed, the discrimination achieved with set 2 (five parameters) is similar, or even slightly higher than the one reached with set 3 (six parameters). One explanatory hypothesis is that while Set 3 uses parameters which describe only one aspect of population morphometry, the distributions of shape (solidity and circularity), Set 2 uses parameters which describe two rather different aspects: the distribution of size and general geometry (fractal dimension and lacunarity). Overall, it appears from this study that parameters describing various aspects of population morphometry should be used in order to improve the efficiency of these classification procedures. The rate of correct classification reaches high values (around 90%); discriminant analyses could therefore be applied in the future to reliably classify populations of microstructures based on their population morphology.

4.2 | Relevance of population morphometry for life detection studies

4.2.1 | Application to test microfossil assemblages

Size distributions in microfossil assemblages have been used previously as a biogenicity criterion in micropaleontological studies (Barghoorn & Tyler, 1965; Butterfield & Chandler, 1992; Knoll & Barghoorn, 1977; Köhler & Heubeck, 2019; Schopf & Barghoorn, 1967; Schopf et al., 2010; Sugitani et al., 2007, 2010, 2013; Wacey et al., 2011). In these studies, the absolute range of sizes and the relative width of size distributions (quantified in our study by the mean/*SD* parameter) were particularly discussed. Qualitatively, the similarity and continuity of shapes (shape distributions in our study) in a population were also proposed as a criterion of biogenicity

(Brasier & Wacey, 2012; Buick, 1990; Schopf et al., 2010). However, as noted by Brasier and Wacey (2012), the morphospaces occupied by biological and relevant abiogenic populations have hardly, if ever, been compared quantitatively.

The current study is a proof of concept exploring the general feasibility and potential of population morphometry. It relies on modern, controlled samples, including modern microbial mats. Can the results of this study be applied directly to microfossil communities in the Precambrian rock record? To answer this, the method was tested on a well-known Proterozoic microfossil assemblage from the 1.0 Ga Angmaat Formation, Bylot Group, Baffin Island, Canada. For the different microfossil populations from this formation that were used in this study, solidity appears to be independent of size, a feature shared with non-colonial morphotypes in modern microbial communities and biomorphs (compare Figure 10a and Figure S15 with Figure 7a). Similarly, for the smaller size ranges, circularity is independent of size, a feature shared only with modern microbial communities here (Compare Figure S15—normalized size under 0.5—with Figure 7b). The independence of size and shape in microbial communities therefore appears to have the potential of being preserved through time by fossilization processes. The large mosaics of microfossil populations (T1 and T2) display size and shape distributions, however, that are very different from modern communities—they are close to those of populations of interstitial spaces (Figure 10b,d,e, hollow squares). In particular, their size distribution does not correspond with the multimodal distribution expected for the populations of different types of non-colonial spheroids in Angmaat Formation (Figures 4a,b and 10b). This may be due to two main problems:

First, in optical microscopy of these natural samples, the contrast between the microfossils and their organic-rich matrix is low, making them difficult to distinguish automatically. This leads to potential errors during image segmentation. Furthermore, many of the microfossils are tightly clumped and are therefore not recognized as individual particles during the segmentation. These critical segmentation-related issues undoubtedly have an effect on measured morphometric characteristics.

Second, there are important spatial heterogeneities in the state of preservation of the individual microfossils, even in a relatively well-preserved rock as the Angmaat Formation (Manning-Berg et al., 2019). Individual microfossils may be partially degraded and have lost their original morphology. Also, the nature of the microbial strains may affect the quality of the preservation of shape. For example, only one relatively resistant strain may have been preserved within a complex initial community. A primary multimodal statistical distribution would then have turned into a unimodal one. It is anticipated that in more strongly altered rocks the shape of cells would be even further altered, affecting the original morphometry of the fossilized microbial community.

In order to test the contribution of these problems, a zoom-in image T2-sub was selected from T2. This image represents a region that is less heterogeneous in terms of state of degradation and has a higher contrast between microfossils and matrix, making the

segmentation of higher quality. We note however that microfossils are still tightly clumped in this area, preventing in places their recognition as individual particles. For this population, the distributions of shapes are very close to those of modern microbial communities (Figure 10a,d,e, hollow stars), confirming the potential influence of degradational heterogeneities and/or contrasting issues. In contrast, the size distribution still differs from the one expected for modern microbial communities (Figure S15). It appears that the clumping of microfossils affected size distributions more than shape distributions.

Discriminant analyses do not attribute the three studied populations of the Angmaat Formation to the system of microbial communities (Figure 10f; Figure S15J,K,L). But consistently with the fact that T2-sub has circularity and solidity distributions close to microbial communities, a discriminant analysis run with Set 3 parameters (only parameters describing distributions of solidity and circularity) attributes T2-sub to microbial communities. Overall, these results suggest that discriminant analyses only work if sets of parameters are chosen that are least likely to be affected by diagenesis. It remains to be determined in future studies how diagenesis, metamorphism, and metasomatism precisely affect population morphometry of microfossil assemblages.

4.2.2 | Sensitivity to image treatment

Image treatment is a critical step in population morphometry. Problems linked to image segmentation can lead to (a) imperfect reproduction of the outlines of the objects, (b) clumping of different objects (e.g., when they are overlapping) into a single particle, and/or (c) erroneous segmentation of objects/areas of the image that do not belong to the system of relevance ("contamination"). All of these issues lead to a discrepancy between observed objects and segmented particles.

The purpose of segmentation is to separate all and only the objects of interest from their background. In the current study, the quality of segmentation depends mainly on the choice of (a) the graylevel threshold and (b) the size threshold. During image segmentation, these thresholds are adjusted manually. Optimal segmentation is reached when there is a maximal equivalence between observed objects and segmented particles. The sensitivity of segmentation—and subsequently, of morphometric measurements—to threshold adjustment was evaluated for one specific image in Figure S16 (segmentation), Figures S17 and S18A,B (morphometric measurements). Figure S16 illustrates that an increase in graylevel threshold creates "contaminant" particles and increases clumping in the segmented image. Increasing the size threshold allows to remove small contaminant particles, but increases the risk of removing objects of interest. Subsequent morphometric measurements are affected by changes in threshold (an example for size distributions is shown in Figure S17). Due to the clumping into large particles and the appearance of small contaminant particles, increases in graylevel threshold stretch the distribution

to lower and higher values (evolution of histograms from left to right in Figure S17). The increase in size threshold also modifies the shape of the size distribution by removing smaller sized particles (evolution of histograms from bottom to top on Figure S17).

The comparison between the source image and the segmented images in Figure S16 shows that the highest segmentation quality is obtained for graylevel thresholds of 100 and 150 and a size threshold of 500 square pixels. At these values, the sensitivity of the segmentation and of morphometric measurements to changes in graylevel threshold is small (compare the two central columns in Figures S16 and S17; compare values at 100 and 150 in Figure S18B,C). However, the segmentation and morphometric measurements appear more sensitive to changes in size threshold (compare lines 1 to 3 in Figures S16 and S17; compare cyan, green, and red curves in Figure S18A,B). In general, these observations, and in particular the threshold intervals for which morphometric measurements are less sensitive, vary among the images. Sensitivity to the threshold choice depends strongly on the source image and on the initial contrast between the objects of interest and their background. The segmentation of microfossil assemblage images, in particular, is more sensitive to changes of thresholding than most others (see Figure S18C–F). However, in the current study, it must be noted that the two images of interstitial spaces for which the segmentation was imperfect (see Section 2.1.1) display the same morphometric trends as the other images of interstitial spaces (Table 1; Figure 8; Figures S1, S2, S11, S12 and S13). This means that final morphometric measurements, to a certain extent, are robust regarding the quality of segmentation.

The threshold that is eventually chosen is the one which optimizes the equivalence between observed objects and segmented particles (Figure S16). In the future, in order to improve the quality of image segmentation, it will be necessary to use (a) alternative imaging techniques, for example, fluorescence-based ones, which increase the contrast between the objects of interest and their surroundings, or 3D imaging, which would separate overlapping particles and (b) use specific image treatment methods, such as local thresholding.

4.2.3 | General guidelines and limits of population morphometry for life detection

The parameters used in this study to characterize particles or populations of particles (size, circularity, solidity, fractal dimension, lacunarity) are universally applicable. Several criteria, such as the shape of distributions (mean/SD, skewness, kurtosis), or the relationship between shape and normalized size, are also independent of the absolute shapes or sizes. As a result, the approach of this study is highly relevant to the Early Life or Extraterrestrial Life studies, since those are contexts where the sizes and shapes are difficult to predict.

Although the objects considered in this study are three-dimensional, two-dimensional pictures were used. An important part of

the structural information is therefore lost: (a) Overlapping particles are not separated and (b) a single plane does not properly describe an anisotropic population. This study, however, is a first proof of concept. For practical reasons, 2D-images were used, since they are much easier to acquire and to treat than, for example, 3D-tomograms. Moreover, micropaleontology data reported in literature most often consist of 2D-images. The goal is thus to create a rapid tool that can be readily applied to images in literature, or can be directly applied to any microscope image. In order to minimize the issue of particle separation during picture analysis, the pictures in this study were specifically chosen that have a small amount of overlapping particles. The issue of anisotropy in a population, however, could not easily be solved. The general methodology described here will be extended to three-dimensional data in the future.

In order to apply this kind of statistical analysis to a population of particles in an image, several conditions must be fulfilled. (a) The objects of interest in the image must be discernible from their background and have clear boundaries. Blurry or poorly contrasted images may strongly alter the signal of interest during treatment. (b) The objects of interest must be discernable from each other. If all the objects are clumped together in a large mass, no reliable information can be derived. Therefore, individual particles must be recognizable. Other types of analysis (e.g., network analysis) must be developed for very dense communities such as bundles formed by filamentous strains. (c) In order to facilitate interpretation, the considered objects should all originate from the same system. A mixture of objects coming from different systems will obscure the signal and/or lead to erroneous interpretations. (d) A sufficient amount of particles must be available in the image for statistical analysis. In this study, it was found that ~100 particles constitute a lower boundary; below this number, the statistic distributions are inaccurate representations of the population. (e) For now, spatial heterogeneities should be minimal. The influence of the scale of study on statistic morphometry was not systematically assessed in the current study and will be the object of future research.

The methodology presented here discriminates specific biologic and abiogenic systems: microbial communities of cells, silica-carbonate biomorphs, and interstitial spaces in clastic fabrics. This choice of systems is of course not absolute. The methodology presented here could be expanded to other systems. In particular, it would be of interest to study populations of other types of organic and/or mineral biomorphs (carbon–sulfur aggregates, manganese oxide precipitates, core-shell aggregates—Cosmidis & Templeton, 2016; Liu et al., 2011; Muscente et al., 2018)—or other types of interstitial spaces—such as in botryoidal or spherulitic chert fabrics (Brasier et al., 2002, 2005). In general, it is critical to have geological knowledge of a sample before applying this method. The abiogenic and biologic hypotheses must be known and defined carefully before statistic approaches can be used to discriminate them. Besides, in this study, although samples of different nature and origins were chosen (see Section 2.1), only a limited amount of images were used to describe every system

(10/11 images for each system). Therefore, the entire morphometric range of each system is certainly far from being entirely represented. For example, microbial communities with a fundamentally different composition and/or ecology may present different morphometric characteristics. This imperfection is mainly due to the difficulty to access (and treat) a large amount of geologically/biologically relevant data from various sources. An increase in the volume and the diversity of treated images would certainly improve the robustness of an automated discrimination algorithm as presented in this study.

5 | CONCLUSION

Morphometric characteristics (size, circularity, solidity, fractal dimension, and lacunarity) were determined for example populations of microstructures of two abiogenic systems (interstitial spaces in clastic rocks, silica-carbonate biomorphs) and one biologic system (microbial communities). At the scale of single populations, it appears that the relationship between the shape of particles (circularity and solidity) and their size allows the consistent distinction of the three systems. At the scale of several populations, the shapes of statistic distributions of size, circularity, and solidity, described here by their mean/*SD*, skewness, and kurtosis, show significant differences between the three systems. Some correlations between these parameters call for future exploration. It is found that discriminant analyses realized with the distribution descriptors of size and shape efficiently separate the three groups of populations in 2D-spaces. Using these discriminant analyses, populations from these three systems can be classified automatically with great accuracy. The same morphometric characterization was applied to assemblages of microfossils from the well-preserved 1.0 Ga Angmaat Formation, Baffin Island, Canada. In these assemblages, biologic size and shape distributions are affected by (spatially heterogeneous) diagenesis and by the presence of abiogenic objects such as interstitial spaces. However, the relationship between size and shape appears to be a biogenic characteristic well preserved in this context. Given the wide applicability of the performed measurements and the very general nature of the observed trends, statistical morphometric analyses appear promising for the identification of microbial remnants in various contexts; they could complement other existing lines of evidence (geologic setting, composition, etc.). This approach can potentially be applied to identify traces of life on other planets, such as Mars. Noticeably, this study extends the concept of morphospace (Raup, 1967) to the population level. Population- or system-scale morphometry could help in the future to get a better understanding of the morphogenetic controls specific to microbial life.

and Innovation Program (grant agreement no. 646894 to MVZ) and under the ERC Seventh Framework Programme FP7/2007-2013 (grant agreement no. 340863 to JMG-R). JMG-R also acknowledges the Ministerio de Economía y Competitividad of Spain through the project CGL2016-78971-P. We are grateful to seven anonymous reviewers for their helpful comments. We thank four anonymous reviewers for their useful comments which greatly improved a previous version of the manuscript. This is IPGP contribution n°4098.

CONFLICT OF INTEREST

The authors declare that there is no conflict of interest regarding the publication of this article.

ORCID

Joti Rouillard https://orcid.org/0000-0002-7335-1536
Juan Manuel García-Ruiz https://orcid.org/0000-0002-4743-8718
Sami Nabhan https://orcid.org/0000-0001-7399-5131
Jian Gong https://orcid.org/0000-0001-7214-1628
Mark A. van Zuilen https://orcid.org/0000-0001-6723-6366

REFERENCES

Abramoff, M., Magalhaes, M., & Ram, S. (2004). Image processing with ImageJ. *Biophotonics International*, *11*, 36–42.

Adams, D. C., & Otárola-Castillo, E. (2013). geomorph: An R package for the collection and analysis of geometric morphometric shape data. *Methods in Ecology and Evolution*, *4*, 393–399.

Adams, D. C., Rohlf, F. J., & Slice, D. E. (2004). Geometric morphometrics: Ten years of progress following the 'revolution'. *Italian Journal of Zoology*, *71*, 5–16. https://doi.org/10.1080/11250000409356545

Aguilera, J. M. (2005). Why food microstructure? *Journal of Food Engineering*, *67*, 3–11. https://doi.org/10.1016/j.jfoodeng.2004.05.050

Arganda-Carreras, I., Kaynig, V., Rueden, C., Eliceiri, K. W., Schindelin, J., Cardona, A., & Sebastian Seung, H. (2017). Trainable Weka segmentation: A machine learning tool for microscopy pixel classification. *Bioinformatics*, *33*, 2424–2426. https://doi.org/10.1093/bioinformatics/btx180

Ausmees, N., Kuhn, J. R., & Jacobs-Wagner, C. (2003). The bacterial cytoskeleton: An intermediate filament-like function in cell shape. *Cell*, *115*, 705–713. https://doi.org/10.1016/S0092-8674(03)00935-8

Baghekema, S. G. L., Lepot, K., Riboulleau, A., Fadel, A., Trentesaux, A., & El Albani, A. (2017). Nanoscale analysis of preservation of ca. 2.1 Ga old Francevillian microfossils, Gabon. *Precambrian Research*, *301*, 1–18. https://doi.org/10.1016/j.precamres.2017.08.024

Barghoorn, E. S., & Tyler, S. A. (1965). Microorganisms from the Gunflint Chert. *Science, New Series*, *147*, 563–577.

Bishop, C. M. (2006). *Pattern recognition and machine learning. Information science and statistics*. New York, NY: Springer.

Bishop, Y., Fienberg, S., & Holland, P. (2007). *Discrete multivariate analysis*. New York: Springer.

Booth-Gauthier, E. A., Du, V., Ghibaudo, M., Rape, A. D., Dahl, K. N., & Ladoux, B. (2013). Hutchinson-Gilford progeria syndrome alters nuclear shape and reduces cell motility in three dimensional model substrates. *Integrative Biology*, *5*, 569. https://doi.org/10.1039/c3ib20231c

Bora, E., Fornito, A., Pantelis, C., & Yücel, M. (2012). Gray matter abnormalities in Major Depressive Disorder: A meta-analysis of voxel based morphometry studies. *Journal of Affective Disorders*, *138*, 9–18. https://doi.org/10.1016/j.jad.2011.03.049

Brasier, M. D., Antcliffe, J., Saunders, M., & Wacey, D. (2015). Changing the picture of Earth's earliest fossils (3.5–1.9 Ga) with new approaches and new discoveries. *Proceedings of the National Academy of Sciences of the United States of America*, *112*, 4859–4864. https://doi.org/10.1073/pnas.1405338111

Brasier, M. D., Green, O. R., Jephcoat, A. P., Kleppe, A. K., Van Kranendonk, M. J., Lindsay, J. F., … Grassineau, N. V. (2002). Questioning the evidence for Earth's oldest fossils. *Nature*, *416*, 76–81. https://doi.org/10.1038/416076a

Brasier, M. D., Green, O. R., Lindsay, J. F., Mcloughlin, N., Steele, A., & Stoakes, C. (2005). Critical testing of Earth's oldest putative fossil assemblage from the ~3. 5 Ga Apex chert, Chinaman Creek, Western Australia. *Precambrian Research*, *140*, 55–102. https://doi.org/10.1016/j.precamres.2005.06.008

Brasier, M. D., Green, O. R., Lindsay, J. F., McLoughlin, N., Stoakes, C. A., Brasier, A. T., & Wacey, D. (2011). *Geology and putative microfossil assemblage of the ca. 3460 Ma "Apex Chert", Western Australia – A field and petrographic guide*. Perth, Australia: Geological Survey of Western Australia.

Brasier, M. D., & Wacey, D. (2012). Fossils and astrobiology: New protocols for cell evolution in deep time. *International Journal of Astrobiology*, *11*, 217–228.

Buick, R. (1990). Microfossil recognition in Archean rocks: An appraisal of spheroids and filaments from a 3500 M.Y. old chert-barite unit at north pole, Western Australia. *Palaios*, *5*, 441–459. https://doi.org/10.2307/3514837

Butterfield, N. J., & Chandler, F. W. (1992). Palaeoenvironmental distribution of Proterozoic microfossils, with an example from the Agu Bay Formation, Baffin Island. *Paleontology*, *35*, 943–957.

Carnerup, A. (2007). *Biomorphs: morphology, chemistry, and implications for the identification of early life*.

Collins, T. (2007). ImageJ for microscopy. *BioTechniques*, *43*, S25–S30. https://doi.org/10.2144/000112517

Cosmidis, J., & Templeton, A. S. (2016). Self-assembly of biomorphic carbon/sulfur microstructures in sulfidic environments. *Nature Communications*, *7*, 12812. https://doi.org/10.1038/ncomms12812

Crisp, D. J., & Williams, R. (1971). Direct measurement of pore-size distribution on artificial and natural deposits and prediction of pore space accessible to interstitial organisms. *Marine Biology*, *10*, 214–226. https://doi.org/10.1007/BF00352810

Curtis, M. E., Sondergeld, C. H., Ambrose, R. J., & Rai, C. S. (2012). Microstructural investigation of gas shales in two and three dimensions using nanometer-scale resolution imaging. *AAPG Bulletin*, *96*, 665–677. https://doi.org/10.1306/08151110188

Delarue, F., Robert, F., Tartèse, R., Sugitani, K., Tang, Q., Duhamel, R., … Xiao, S. (2018). Can NanoSIMS probe quantitatively the geochemical composition of ancient organic-walled microfossils? A case study from the early Neoproterozoic Liulaobei Formation. *Precambrian Research*, *311*, 65–73. https://doi.org/10.1016/j.precamres.2018.03.003

Delarue, F., Rouzaud, J.-N., Derenne, S., Bourbin, M., Westall, F., Kremer, B., … Robert, F. (2016). The Raman-derived carbonization continuum: A tool to select the best preserved molecular structures in Archean kerogens. *Astrobiology*, *16*, 407–417. https://doi.org/10.1089/ast.2015.1392

Diamond, S. (1970). Pore size distributions in clays. *Clays and Clay Minerals*, *18*, 7–23. https://doi.org/10.1346/CCMN.1970.0180103

Domingos, P. (2012). A few useful things to know about machine learning. *Communications of the ACM*, *55*, 78. https://doi.org/10.1145/2347736.2347755

Doube, M., Kłosowski, M. M., Arganda-Carreras, I., Cordelières, F. P., Dougherty, R. P., Jackson, J. S., … Shefelbine, S. J. (2010). BoneJ: Free and extensible bone image analysis in ImageJ. *Bone*, *47*, 1076–1079. https://doi.org/10.1016/j.bone.2010.08.023

Eberl, D. D., Drits, V. A., & Srodon, J. (1998). Deducing growth mechanisms for minerals from the shapes of crystal size distribution. *American Journal of Science*, *298*, 499–533.

Etemad, K., & Chellappa, R. (1997). Discriminant analysis for recognition of human face images. *Journal of the Optical Society of America A*, *14*, 1724–1733. https://doi.org/10.1364/JOSAA.14.001724

Fadel, A., Lepot, K., Busigny, V., Addad, A., & Troadec, D. (2017). Iron mineralization and taphonomy of microfossils of the 2.45–2.21 Ga Turee Creek Group, Western Australia. *Precambrian Research*, *298*, 530–551. https://doi.org/10.1016/j.precamres.2017.07.003

Farina, A., Kovacs-Vajna, Z. M., & Leone, A. (1999). Fingerprint minutiae extraction from skeletonized binary images. *Pattern Recognition*, *32*, 877–889. https://doi.org/10.1016/S0031-3203(98)00107-1

Ferreira, T. A., Blackman, A. V., Oyrer, J., Jayabal, S., Chung, A. J., Watt, A. J., … van Meyel, D. J. (2014). Neuronal morphometry directly from bitmap images. *Nature Methods*, *11*, 982–984. https://doi.org/10.1038/nmeth.3125

Fusseis, F., Schrank, C., Liu, J., Karrech, A., Llana-Fúnez, S., Xiao, X., & Regenauer-Lieb, K. (2012). Pore formation during dehydration of a polycrystalline gypsum sample observed and quantified in a time-series synchrotron X-ray micro-tomography experiment. *Solid Earth*, *3*, 71–86. https://doi.org/10.5194/se-3-71-2012

García-Ruiz, J. M., Carnerup, A., Christy, A. G., Welham, N. J., & Hyde, S. T. (2002). Morphology: An ambiguous indicator of biogenicity. *Astrobiology*, *2*, 353–369. https://doi.org/10.1089/153110702762027925

García-Ruiz, J. M., Hyde, S. T., Carnerup, A. M., Christy, A. G., Kranendonk, M. J. V., & Welham, N. J. (2003). Self-assembled silica-carbonate structures and detection of ancient microfossils. *Science*, *302*, 1194–1197. https://doi.org/10.1126/science.1090163

García-Ruiz, J. M., Nakouzi, E., Kotopoulou, E., Tamborrino, L., & Steinbock, O. (2017). Biomimetic mineral self-organization from silica-rich spring waters. *Science Advances*, *3*. https://doi.org/10.1126/sciadv.1602285

Gérard, E., Ménez, B., Couradeau, E., Moreira, D., Benzerara, K., Tavera, R., & López-García, P. (2013). Specific carbonate–microbe interactions in the modern microbialites of Lake Alchichica (Mexico). *The ISME Journal*, *7*, 1997–2009. https://doi.org/10.1038/ismej.2013.81

Guo, Z., Peng, X., Czaja, A. D., Chen, S., & Ta, K. (2018). Cellular taphonomy of well-preserved Gaoyuzhuang microfossils: A window into the preservation of ancient cyanobacteria. *Precambrian Research*, *304*, 88–98. https://doi.org/10.1016/j.precamres.2017.11.007

Harvey, R. J., & Marr, A. G. (1966). Measurement of size distributions of bacterial cells. *Journal of Bacteriology*, *92*, 805–811.

Hofmann, H. J., & Jackson, G. D. (1991). Shelf-facies microfossils from the Uluksan Group (Proterozoic Bylot Supergroup), Baffin Island, Canada. *Journal of Paleontology*, *65*, 361–382. https://doi.org/10.1017/S0022336000030353

Holt, K., Allen, G., Hodgson, R., Marsland, S., & Flenley, J. (2011). Progress towards an automated trainable pollen location and classifier system for use in the palynology laboratory. *Review of Palaeobotany and Palynology*, *167*, 175–183. https://doi.org/10.1016/j.revpalbo.2011.08.006

House, C. H., Oehler, D. Z., Sugitani, K., & Mimura, K. (2013). Carbon isotopic analyses of ca. 3.0 Ga microstructures imply planktonic autotrophs inhabited Earth's early oceans. *Geology*, *41*, 651–654. https://doi.org/10.1130/G34055.1

Ingber, D. E. (2003). Tensegrity I. Cell structure and hierarchical systems biology. *Journal of Cell Science*, *116*, 1157–1173. https://doi.org/10.1242/jcs.00359

Ioannidis, M. A., & Chatzis, I. (1993). Network modelling of pore structure and transport properties of porous media. *Chemical Engineering Science*, *48*, 951–972. https://doi.org/10.1016/0009-2509(93)80333-L

Javaux, E. J., Knoll, A. H., & Walter, M. R. (2004). TEM evidence for eukaryotic diversity in mid-Proterozoic oceans. *Geobiology*, *2*, 121–132. https://doi.org/10.1111/j.1472-4677.2004.00027.x

Jones, L. J., Carballido-López, R., & Errington, J. (2001). Control of cell shape in bacteria: Helical, actin-like filaments in Bacillus subtilis. *Cell*, *104*, 913–922. https://doi.org/10.1016/S0092-8674(01)00287-2

Kah, L. C., & Knoll, A. H. (1996). Microbenthic distribution of Proterozoic tidal flats: Environmental and taphonomic considerations. *Geology*, *24*, 79–82. https://doi.org/10.1130/0091-7613(1996)024<0079:MDOPTF>2.3.CO;2

Kah, L. C., Sherman, A. G., Narbonne, G. M., Knoll, A. H., & Kaufman, A. J. (1999). Supergroup, Baffin Island, Canada: implications for regional lithostratigraphic correlations, *36*, 20.

Karakas, S., & Kavaklı, A. (2005). Morphometric examination of the paranasal sinuses and mastoid air cells using computed tomography. *Annals of Saudi Medicine*, *25*(1), 41–45. https://doi.org/10.5144/0256-4947.2005.41

Katz, A., Alimova, A., Xu, M., Rudolph, E., Shah, M. K., Savage, H. E., … Alfano, R. R. (2003). Bacteria size determination by elastic light scattering. *IEEE Journal of Selected Topics in Quantum Electronics*, *9*, 277–287. https://doi.org/10.1109/JSTQE.2003.811284

Kempe, A., Wirth, R., Altermann, W., Stark, R. W., Schopf, J. W., & Heckl, W. M. (2005). Focussed ion beam preparation and in situ nanoscopic study of Precambrian acritarchs. *Precambrian Research*, *140*, 36–54. https://doi.org/10.1016/j.precamres.2005.07.002

Kile, D. E., Eberl, D. D., Hoch, A. R., & Reddy, M. M. (2000). An assessment of calcite crystal growth mechanisms based on crystal size distributions. *Geochimica et Cosmochimica Acta*, *64*, 2937–2950. https://doi.org/10.1016/S0016-7037(00)00394-X

Knoll, A. H., & Barghoorn, E. S. (1977). Archean microfossils showing cell division from the Swaziland system of South Africa. *Science*, *198*, 396–398. https://doi.org/10.1126/science.198.4315.396

Knoll, A. H., Worndle, S., & Kah, L. C. (2013). Covariance of microfossil assemblages and microbialite textures across an upper mesoproterozoic carbonate platform. *Palaios*, *28*, 453–470. https://doi.org/10.2110/palo.2013.p13-005r

Koch, A. L. (1966). Distribution of cell size in growing cultures of bacteria and the applicability of the collins-richmond principle. *Journal of General Microbiology*, *45*, 409–417.

Köhler, I., & Heubeck, C. (2019). Microbial-mat-associated tephra of the Archean Moodies Group, Barberton Greenstone Belt (BGB), South Africa: Resemblance to potential biostructures and ecological implications. *South African Journal of Geology*, *122*(2), 221–236. https://doi.org/10.25131/sajg.122.0015

Kuila, U., & Prasad, M. (2013). Specific surface area and pore-size distribution in clays and shales: Specific surface area and pore-size distribution in clays and shales. *Geophysical Prospecting*, *61*, 341–362. https://doi.org/10.1111/1365-2478.12028

Lepot, K., Addad, A., Knoll, A. H., Wang, J., Troadec, D., Béché, A., & Javaux, E. J. (2017). Iron minerals within specific microfossil morphospecies of the 1.88 Ga Gunflint Formation. *Nature Communications*, *8*, 14890.

Liu, J., Qiao, S. Z., Chen, J. S., (David) Lou, X. W., Xing, X., & (Max) Lu, G. Q. (2011). Yolk/shell nanoparticles: New platforms for nanoreactors, drug delivery and lithium-ion batteries. *Chemical Communications*, *47*, 12578. https://doi.org/10.1039/c1cc13658e

Loucks, R. G., Reed, R. M., Ruppel, S. C., & Jarvie, D. M. (2009). Morphology, genesis, and distribution of nanometer-scale pores in siliceous mudstones of the Mississippian Barnett shale. *Journal of Sedimentary Research*, *79*, 848–861. https://doi.org/10.2110/jsr.2009.092

MacLeod, N., Benfield, M., & Culverhouse, P. (2010). Time to automate identification. *Nature*, *467*, 154–155. https://doi.org/10.1038/467154a

Manning-Berg, A., Wood, R., Williford, K., Czaja, A., & Kah, L. (2019). The taphonomy of proterozoic microbial mats and implications for early diagenetic silicification. *Geosciences*, *9*, 40. https://doi.org/10.3390/geosciences9010040

McLachlan, G. J. (2004). *Discriminant analysis and statistical pattern recognition*. Hoboken, NJ: Wiley series in probability and statistics.

McMahon, S. (1916). Earth's earliest and deepest purported fossils may be iron-mineralized chemical gardens. *Proceedings of the Royal Society B: Biological Sciences.*, 2019(286), 20192410.

Melero-García, E., Santisteban-Bailón, R., & García-Ruiz, J. M. (2009). Role of bulk pH during witherite biomorph growth in silica gels. *Crystal Growth and Design*, 9, 4730–4734. https://doi.org/10.1021/cg9005967

Młynarczuk, M., Górszczyk, A., & Ślipek, B. (2013). The application of pattern recognition in the automatic classification of microscopic rock images. *Computers & Geosciences*, 60, 126–133. https://doi.org/10.1016/j.cageo.2013.07.015

Montalti, M., Zhang, G., Genovese, D., Morales, J., Kellermeier, M., & García-Ruiz, J. M. (2017). Local pH oscillations witness auto-catalytic self-organization of biomorphic nanostructures. *Nature Communications*, 8, 14427. https://doi.org/10.1038/ncomms14427

Muscente, A. D., Czaja, A. D., Tuggle, J., Winkler, C., & Xiao, S. (2018). Manganese oxides resembling microbial fabrics and their implications for recognizing inorganically preserved microfossils. *Astrobiology*, 18, 249–258. https://doi.org/10.1089/ast.2017.1699

Pang, K., Tang, Q., Schiffbauer, J. D., Yao, J., Yuan, X., Wan, B., ...Xiao, S. (2013). The nature and origin of nucleus-like intracellular inclusions in Paleoproterozoic eukaryote microfossils. *Geobiology*, https://doi.org/10.1111/gbi.12053

Papadopulos, F., Spinelli, M., Valente, S., Foroni, L., Orrico, C., Alviano, F., & Pasquinelli, G. (2007). Common tasks in microscopic and ultra-structural image analysis using ImageJ. *Ultrastructural Pathology*, 31, 401–407. https://doi.org/10.1080/01913120701719189

Pedregosa, F., Varoquaux, G., Gramfort, A., Michel, V., Thirion, B., Grisel, O., ... Cournapeau, D. (2011). Scikit-learn: Machine learning in python. *Journal of Machine Learning Research*, 12, 6.

Pinho, M. G., Kjos, M., & Veening, J.-W. (2013). How to get (a)round: Mechanisms controlling growth and division of coccoid bacteria. *Nature Reviews Microbiology*, 11, 601–614. https://doi.org/10.1038/nrmicro3088

Rajkowska, G., Miguel-Hidalgo, J. J., Wei, J., Dilley, G., Pittman, S. D., Meltzer, H. Y., ... Stockmeier, C. A. (1999). Morphometric evidence for neuronal and glial prefrontal cell pathology in major depression∗. *Biological Psychiatry*, 45, 1085–1098.

Rappaz, B., Marquet, P., Cuche, E., Emery, Y., Depeursinge, C., & Magistretti, P. J. (2005). Measurement of the integral refractive index and dynamic cell morphometry of living cells with digital holographic microscopy. *Optics Express*, 13, 9361–9373. https://doi.org/10.1364/OPEX.13.009361

Raup, D. M. (1967). Geometric analysis of shell coiling: Coiling in Ammonoids. *Journal of Paleontology*, 41, 43–65.

Robert, C. (2014). Machine learning, a probabilistic perspective. *Chance*, 27, 62–63.

Rouillard, J., García-Ruiz, J.-M., Gong, J., & van Zuilen, M. A. (2018). A morphogram for silica-witherite biomorphs and its application to microfossil identification in the early earth rock record. *Geobiology*, 16, 279–296. https://doi.org/10.1111/gbi.12278

Schopf, J. W. (1983). *Earth's earliest biosphere: Its origin and evolution*. Princeton, NJ: Princeton University Press.

Schopf, J. W. (1993). Microfossils of the early Archean apex chert: New evidence of the antiquity of life. *Science, New Series*, 260, 640–646. https://doi.org/10.1126/science.260.5108.640

Schopf, J. W., & Barghoorn, E. S. (1967). Alga-like fossils from the early Precambrian of South Africa. *Science*, 156, 508–512. https://doi.org/10.1126/science.156.3774.508

Schopf, J. W., Kitajima, K., Spicuzza, M. J., Kudryavtsev, A. B., & Valley, J. W. (2018). SIMS analyses of the oldest known assemblage of microfossils document their taxon-correlated carbon isotope compositions. *Proceedings of the National Academy of Sciences of the United States of America*, 115, 53–58. https://doi.org/10.1073/pnas.1718063115

Schopf, J. W., & Kudryavtsev, A. B. (2009). Confocal laser scanning microscopy and Raman imagery of ancient microscopic fossils. *Precambrian Research*, 173, 39–49. https://doi.org/10.1016/j.precamres.2009.02.007

Schopf, J. W., & Kudryavtsev, A. B. (2012). Biogenicity of Earth's earliest fossils: A resolution of the controversy. *Gondwana Research*, 22, 761–771.

Schopf, J. W., Kudryavtsev, A. B., Agresti, D. G., Wdowiak, T. J., & Czaja, A. D. (2002). Laser-Raman imagery of Earth's earliest fossils. *Nature*, 416, 73–76. https://doi.org/10.1038/416073a

Schopf, J. W., Kudryavtsev, A. B., Sugitani, K., & Walter, M. R. (2010). Precambrian microbe-like pseudofossils: A promising solution to the problem. *Precambrian Research*, 179, 191–205.

Snoek, J., Larochelle, H., & Adams, R. P. (2012). Practical Bayesian optimization of machine learning algorithms. In: F. Pereira, C. J. C. Burges, L. Bottou & K. Q. Weinberger (Eds). *Advances in neural information processing systems* (pp. 2951–2959). Presented at the Neural Information Processing Systems. Lakeville, Minnesota: Curran Associates Inc.

Srinivasa Vittala, S., Govindaiah, S., & Honne Gowda, H. (2004). Morphometric analysis of sub-watersheds in the pavagada area of Tumkur district, South India using remote sensing and gis techniques. *Journal of the Indian Society of Remote Sensing*, 32, 351–362. https://doi.org/10.1007/BF03030860

Sugitani, K., Grey, K., Allwood, A., Nagaoka, T., Mimura, K., Minami, M., ... Walter, M. R. (2007). Diverse microstructures from Archaean chert from the Mount Goldsworthy-Mount Grant area, Pilbara Craton, Western Australia: Microfossils, dubiofossils, or pseudofossils? *Precambrian Research*, 158, 228–262. https://doi.org/10.1016/j.precamres.2007.03.006

Sugitani, K., Kohama, T., Mimura, K., Takeuchi, M., Senda, R., & Morimoto, H. (2018). Speciation of paleoarchean life demonstrated by analysis of the morphological variation of lenticular microfossils from the Pilbara Craton, Australia. *Astrobiology*, 18, 1057–1070. https://doi.org/10.1089/ast.2017.1799

Sugitani, K., Lepot, K., Nagaoka, T., Mimura, K., Kranendonk, M. V., Oehler, D. Z., & Walter, M. R. (2010). Biogenicity of morphologically diverse carbonaceous microstructures from the ca. 3400 Ma strelley pool formation, in the Pilbara Craton, Western Australia. *Astrobiology*, 10.

Sugitani, K., Mimura, K., Nagaoka, T., Lepot, K., & Takeuchi, M. (2013). Microfossil assemblage from the 3400 Ma strelley pool formation in the Pilbara Craton, Western Australia: Results form a new locality. *Precambrian Research*, 226, 59–74.

Tsarenko, P. M. (2006). *Algae of Ukraine: Diversity, nomenclature, taxonomy, ecology and geography*. Ruggell: Gantner Verlag.

Uysal, Z. (2001). Chroococcoid cyanobacteria Synechococcus spp. in the Black Sea: Pigments, size, distribution, growth and diurnal variability. *Journal of Plankton Research*, 23, 175–189. https://doi.org/10.1093/plankt/23.2.175

Vago, J. L., & Westall, F., Pasteur Instrument Teams, Landing, S., Coates, A. J., Jaumann, R., & ... Carreau, C.; the ExoMars Project Team. (2017). Habitability on early mars and the search for biosignatures with the ExoMars rover. *Astrobiology*, 17, 471–510. https://doi.org/10.1089/ast.2016.1533

Wacey, D., Kilburn, M. R., Saunders, M., Cliff, J., & Brasier, M. D. (2011). Microfossils of sulphur-metabolizing cells in 3.4-billion-year-old rocks of Western Australia. *Nature Geoscience*, 4, 698–702. https://doi.org/10.1038/ngeo1238

Wacey, D., Menon, S., Green, L., Gerstmann, D., Kong, C., Mcloughlin, N., ... Brasier, M. (2012). Taphonomy of very ancient microfossils from the ~ 3400 Ma Strelley Pool Formation and ~ 1900 Ma Gunflint Formation : New insights using a focused ion beam. *Precambrian Research*, 220–221, 234–250.

Wacey, D., Saunders, M., Kong, C., Brasier, A., & Brasier, M. (2015). 3.46 Ga Apex chert "microfossils" reinterpreted as mineral artefacts

produced during phyllosilicate exfoliation. *Gondwana Research*, *36*, 296–313. https://doi.org/10.1016/j.gr.2015.07.010

Williford, K. H., Ushikubo, T., Schopf, J. W., Lepot, K., Kitajima, K., & Valley, J. W. (2013). Preservation and detection of microstructural and taxonomic correlations in the carbon isotopic compositions of individual Precambrian microfossils. *Geochimica et Cosmochimica Acta*, *104*, 165–182. https://doi.org/10.1016/j.gca.2012.11.005

Wucherpfennig, T., Hestler, T., & Krull, R. (2011). Morphology engineering-osmolality and its effect on Aspergillus niger morphology and productivity. *Microbial Cell Factories*, *10*, 58. https://doi.org/10.1186/1475-2859-10-58

Zhang, G. (2015). *Morphogenesis of self-assembled crystalline materials of calcium carbonate and silica.*

SUPPORTING INFORMATION

Additional supporting information may be found online in the Supporting Information section.